2018

Upper Mantle Earth Structure in Africa From Full-Wave Ambient Noise Tomography

E. L. Emry

Yang Shen

A. A. Nyblade

A. Flinders

X. Bao

AGU100 ADVANCING EARTH AND SPACE SCIENCE

Geochemistry, Geophysics, Geosystems

RESEARCH ARTICLE
10.1029/2018GC007804

Key Points:
- Full-waveform, long-period ambient noise tomography was used to produce a new isotropic *Vs* model of the upper mantle beneath Africa
- Several cratonic fragments have been imaged in the upper mantle, particularly within the Congo Craton
- Results suggest multiple upwellings beneath Africa, including complex patterns of low-velocity features beneath the East African Rift System

Supporting Information:
- Supporting Information S1
- Data Set S1
- Data Set S2
- Data Set S3
- Data Set S4

Correspondence to:
E. L. Emry,
erica.emry@nmt.edu

Citation:
Emry, E. L., Shen, Y., Nyblade, A. A., Flinders, A., & Bao, X. (2019). Upper mantle Earth structure in Africa from full-wave ambient noise tomography. *Geochemistry, Geophysics, Geosystems*, *20*, 120–147. https://doi.org/10.1029/2018GC007804

Received 2 JUL 2018
Accepted 7 DEC 2018
Accepted article online 11 DEC 2018
Published online 5 JAN 2019

Upper Mantle Earth Structure in Africa From Full-Wave Ambient Noise Tomography

E. L. Emry[1,2,3], Y. Shen[2], A. A. Nyblade[1,4], A. Flinders[2,5], and X. Bao[2]

[1]Department of Geosciences, Pennsylvania State University, University Park, PA, USA, [2]Graduate School of Oceanography, University of Rhode Island, Narragansett, RI, USA, [3]Now at Earth and Environmental Sciences, New Mexico Institute of Mining and Technology, Socorro, NM, USA, [4]School of Geosciences, The University of the Witwatersrand, Johannesburg, South Africa, [5]Now at The United States Geological Survey, Menlo Park, CA, USA

Abstract Our understanding of the tectonic development of the African continent and the interplay between its geological provinces is hindered by unevenly distributed seismic instrumentation. In order to better understand the continent, we used long-period ambient noise full-waveform tomography on data collected from 186 broadband seismic stations throughout Africa and surrounding regions to better image the upper mantle structure. We extracted empirical Green's functions from ambient seismic noise using a frequency-time normalization method and retrieved coherent signal at periods of 7–340 s. We simulated wave propagation through a heterogeneous Earth using a spherical finite-difference approach to obtain synthetic waveforms, measured the misfit as phase delay between the data and synthetics, calculated numerical sensitivity kernels using the scattering integral approach, and iteratively inverted for structure. The resulting images of isotropic, shear wave speed for the continent reveal segmented, low-velocity upper mantle beneath the highly magmatic northern and eastern sections of the East African Rift System (EARS). In the southern and western sections, high-velocity upper mantle dominates, and distinct, low-velocity anomalies are restricted to regions of current volcanism. At deeper depths, the southern and western EARS transition to low velocities. In addition to the EARS, several low-velocity anomalies are scattered through the shallow upper mantle beneath Angola and North Africa, and some of these low-velocity anomalies may be connected to a deeper feature. Distinct upper mantle high-velocity anomalies are imaged throughout the continent and suggest multiple cratonic roots within the Congo region and possible cratonic roots within the Sahara Metacraton.

Plain Language Summary We use advanced seismic imaging techniques (full-waveform tomography), constrained by data from background (ambient) seismic noise to image the upper mantle beneath the African continent and search for low-velocity structures (hot spots) that might coincide with regions of volcanism, surface uplift, and continental rifting, particularly along the East African Rift. We also searched for high-velocity structures (old, rigid blocks) that could influence how warm, buoyant material flows within the Earth's upper mantle. Our seismic tomography method allowed us to obtain a clear image of structure beneath parts of Africa where no or very few seismometers are located (such as the Sahara Desert and the Congo Basin). Our results provide indications for segmented secondary (or shallow) upwellings in the upper mantle beneath East Africa, as opposed to earlier models suggesting one large, continuous plume within the upper mantle. Our results also suggest that the one large, rigid, cratonic block previously imaged beneath the Congo region may instead be composed of smaller, distinct blocks. These results provide insight into the factors that control continental rifting along East Africa and provide new testable models that help us to understand the relationships between upper mantle flow, rifting, volcanism, surface uplift, and sedimentation records.

1. Introduction

The continent of Africa is composed of terranes that have together recorded billions of years of geologic history. Ancient Archean cratons are fringed by regions of deformation associated with earlier continental collisions, aulocogens and associated volcanics stretch inland from earlier continental breakup episodes, and shear zones parallel many regions of earlier tectonic activity (Abdelsalam et al., 2002; Begg et al., 2009; Collins & Piesarevsky, 2005; Porada, 1989). In many instances, the current day tectonic processes, such as rifting along the East African Rift System (EARS), of the continent principally act upon and overprint the weakest

regions that have sustained earlier lithospheric damage (e.g., Corti, 2009; Ebinger et al., 2000, 2017; Keranen et al., 2009).

While some studies suggest that magmatism in the Ethiopian segment of the East African rift results from passive melting of normal mantle (e.g., Hammond et al., 2013; Rychert et al., 2012), a majority of studies suggest that the mantle beneath East Africa is characterized by a deep-seated, low wave speed anomaly, possibly a mantle plume (e.g., Bastow et al., 2008; Benoit, Nyblade, & VanDecar, 2006; French & Romanowicz, 2015; Hansen & Nyblade, 2013; Ritsema et al., 2011). Several studies have suggested that the low wave speed anomaly is thermochemical in nature (Cornwell et al., 2011; Rooney et al., 2012; Thompson et al., 2015). Mantle plumes are expected to affect patterns of uplift and subsidence at the surface, and as such, sedimentary records are also often relevant to the discussion of mantle upwellings (Burke & Gunnell, 2008; Chardon et al., 2018; Hager et al., 1985; Lithgow-Bertelloni & Silver, 1998). This is particularly true for the current-day EARS, the African Superswell, and its possible connection to a deep-seated African Superplume (e.g., Grand, 2000; Nyblade & Robinson, 1994). However, in order to couple the deep with the shallow systems, a strong understanding of present Earth structure is necessary (e.g., Hager et al., 1985; Lithgow-Bertelloni & Silver, 1998).

Numerous continental-scale, regional-scale, and focused tomographic studies, each with their own data and methodology, have already been completed (e.g., Fishwick & Bastow, 2011, and references therein). However, a challenge to deciphering the tomographic results, including the spatial relationships between low-velocity asthenosphere and rigid cratons, is the uneven broadband seismic coverage, which is relatively dense immediately adjacent to much of the EARS, while being notably sparse in regions distant from the rift (Figure 1). Furthermore, the varying scales of individual study, the data that are included, and the methods that are employed influence the resulting resolution, uncertainty, and interpretations of the results (e.g., Bastow, 2012; Rawlinson et al., 2014).

With recent developments in seismic tomography methods, alongside increased availability of high-performance computational resources, we are now able to analyze all together a wealth of previously collected seismic data from Africa with new ambient noise and full-waveform tomography approaches (e.g., Shapiro et al., 2005; Shen et al., 2012; Zhang et al., 2012). In this paper, we extract empirical Green's functions (EGFs) from the vertical component of ambient seismic noise at periods up to 340 s from broadband seismometers located throughout Africa, the Middle East, and southern Europe (Figure 1; Shen et al., 2012). We then numerically calculate synthetic Green's tensors using a 3-D finite-difference wave propagation method (Zhang et al., 2012). These accurate synthetic waveforms are compared directly with the long-period Rayleigh waveforms extracted from ambient noise and the measured phase delays inverted (Paige & Saunders, 1982), incorporating 3-D, numerical sensitivity kernels (Zhao et al., 2005), to obtain absolute, isotropic, upper mantle shear wave speeds throughout continental Africa.

2. Tectonic Background

2.1. African Cratonic Structure

The African continent is composed of several cratons, with Archean rocks outcropping at the surface (Figure 1). Several large cratonic provinces exist: the West African craton, in west-northwest Africa; the Congo Craton, in western Central Africa; the Tanzania Craton, in eastern Central Africa; and the Kalahari, in southern Africa (Begg et al., 2009). Within each of these larger groupings are several smaller Archean/Proterozoic nuclei: the Reguibat and Man-Leo within the West Africa Craton; the Gabon-Kamerun, the Bomu-Kibalan, the Kasai, and the Angolan within the Congo Craton; the Ugandan and distinct terranes of the Tanzanian within the larger Tanzania Craton; and the Zimbabwean and the distinct terranes of the Kaapvaal within the Kalahari Craton (e.g., Begg et al., 2009; Ennih & Liégeois, 2008; Jessell et al., 2016). One markedly different region is the Sahara Metacraton in North Africa, so-named for the widespread deformation and metasomatism that occurred during the Pan-African Orogeny; this altered cratonic region is largely buried beneath the Sahara Desert, making it difficult to study (Abdelsalam et al., 2002; Begg et al., 2009; Liégeois et al., 2013).

The African cratons are bordered by mobile belts, where deformation and metasomatism occurred during previous collisional and extensional events (Figure 1). Several mobile belts contain stranded Archean and

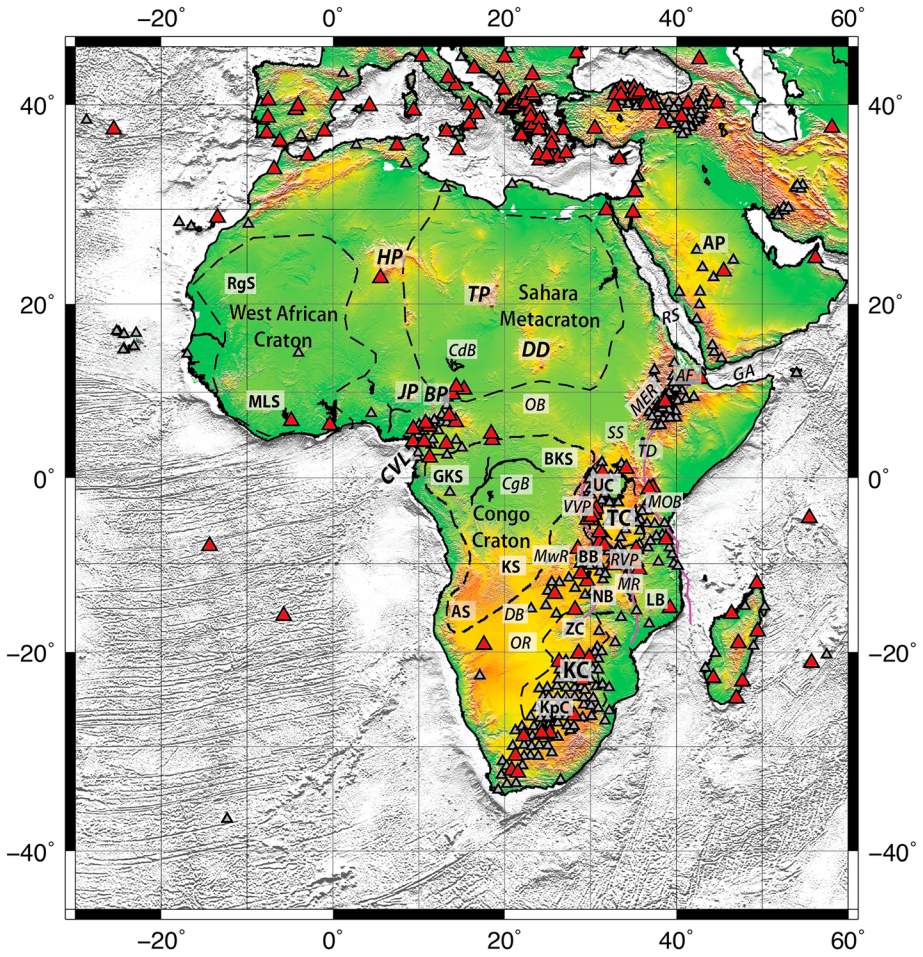

Figure 1. Topography/Bathymetry from ETOPO1 showing land-based broadband seismometer locations (terrain shaded and gray shaded, respectively; Amante & Eakins, 2009). Small gray triangles show all stations for which ambient noise data have been collected and processed. Red triangles indicate stations for which empirical Green's functions with signal-to-noise ratios > 5 have been obtained from long-period ambient noise at 40–340 s and were used in the waveform inversion. Dashed black lines show the estimated boundaries of the larger cratonic regions, including the Sahara Metacraton. Thin, purple lines show segments of the East African Rift System, from Chorowicz (2005). Abbreviations are as follows (alphabetical): *AF* = Afar; AP = Arabian Peninsula; AS = Angolan Shield; BB = Bengweulu Block; BKS = Bomu-Kibalan Shield; *BP* = Biu Plateau; *CdB* = Chad Basin; *CgB* = Congo Basin; *CVL* = Cameroon Volcanic Line; *DB* = Damara Belt; *DD* = Darfur Dome; *GA* = Gulf of Aden; GKS = Gabon-Kamerun Shield; *HP* = Hoggar Plateau; *JP* = Jos Plateau; KC = Kalahari Craton; KpC = Kaapvaal Craton; KS = Kasai Shield; LB = Lurio Block; *MOB* = Mozambique Orogenic Belt; *MER* = Main Ethiopian Rift; MLS = Man-Leo Shield; *MR* = Malawi Rift; *MwR* = Mweru Rift; NB = Niassa Block; *OB* = Oubanguides Belt; *OR* = Okavango Rift; Rgs = Reguibat Shield; *RS* = Red Sea; *RVP* = Rungwe Volcanic Province; *SS* = South Sudan; TC = Tanzania Craton; *TD* = Turkana Depression; *TP* = Tibesti Plateau; UC = Uganda Craton; *VVP* = Virunga Volcanic Province; ZC = Zimbabwe Craton.

Proterozoic fragments within them (e.g., Abdelsalam et al., 2002; Begg et al., 2009). A few such fragments include the Bengweulu, the Lurio, and the Niassa blocks in south central Africa within the Kibaran, Irumide, Southern Irumide, and Lurio belts (Andreoli, 1984; Begg et al., 2009). Such cratonic fragments within the larger mobile belts could still have deep lithospheric roots detectable by geophysical studies. Other large mobile belts include the Oubanguides along the northern side of the Congo and Tanzania Cratons, the Damara Belt between the Congo and Kalahari Cratons, and the Mozambique Orogenic Belt along the eastern side of the Tanzania Craton and the EARS (Begg et al., 2009).

Within several of the cratonic provinces, between exposed Archean nuclei are thick sedimentary basins; in some places these basins are known to have formed during extensional episodes (Ennih & Liégeois, 2008). The Congo Basin is located between the four distinct Archean nuclei on the edges of the larger Congo

Craton (Begg et al., 2009). Although this sedimentary basin exhibits shallow (subbasin) extensional structures (e.g., Kadima et al., 2011), the basin is typically considered intracratonic because of the massive, deep lithospheric root imaged by some seismic tomography studies (e.g., Crosby et al., 2010; Priestley & McKenzie, 2006; Priestley et al., 2008; Ritsema & van Heijst, 2000; Schaeffer & Lebedev, 2013; Sebai et al., 2006; Sicilia et al., 2008). However, other tomographic models have suggested that the Congo Craton may be composed of smaller blocks (Fishwick, 2010; Pasyanos & Nyblade, 2007; Raveloson et al., 2015).

2.2. The East African Rift

The EARS is composed of several rift branches that stretch from the Red Sea and Gulf of Aden in the northeast, along the eastern side of Africa, to Zambia, Madagascar, and Mozambique in the south (e.g., Chorowicz, 2005; Figure 1). Along much of the EARS, rifting closely follows the trend of the mobile zones, particularly in the south where several rigid cratons and cratonic fragments are located (e.g., Begg et al., 2009). The EARS segments are generally narrow ($<$100 km), although the Turkana and Omo regions of northern Kenya and southern Ethiopia are much broader (~300 km); this region is marked by lower elevation and a prior episode of rifting that strikes obliquely to current day rifting (Ebinger et al., 2000). In the north, large flood basalts are located throughout Ethiopia and Yemen, and the oldest volcanic deposits (~45 Myr) are found in the Turkana Depression (Furman, 2007; Furman et al., 2006). In general, the northern EARS and Eastern Branch are more highly magmatic than the Western and Southern Branches (Furman, 2007); this is reinforced by prior research that suggests that the northern EARS is underlain by particularly slow upper mantle velocities (e.g., Bastow et al., 2008; Benoit, Nyblade, Owens, & Stuart , 2006; Benoit, Nyblade, & VanDecar, 2006; Chang & van der Lee, 2011; Dugda et al., 2007; Fishwick, 2010; Gallacher et al., 2016; Sebai et al., 2006). The EARS also coincides with a broad region of high elevations that may be associated with dynamic uplift due to mantle upwellings or thermal alteration (e.g., Lithgow-Bertelloni & Silver, 1998; Mulibo & Nyblade, 2013a; Nyblade & Robinson, 1994).

2.3. North Africa

The geology of North Africa, particularly the Sahara Metacraton, is mostly buried beneath the Sahara Desert (Figure 1). Scattered regions of elevated topography exist throughout North Africa; some of these expose altered Proterozoic or Archean rocks of the Sahara Metacraton and many are capped by Cenozoic volcanic deposits (Abdelsalam et al., 2002; Burke & Gunnell, 2008). These small-scale regions of uplift have been proposed by earlier studies to be due to dynamic uplift (Burke & Gunnell, 2008; Forte et al., 2010). Seismic instrumentation has been very sparse throughout the Sahara (Figure 1). Despite this, earlier seismic studies suggest that North Africa may have lower than average velocities at shallow mantle depths (e.g., Fishwick, 2010) and that several high-velocity regions within may mark the locations of cratonic fragments within the Sahara Metacraton (Liégeois et al., 2013; Pasyanos & Nyblade, 2007; Sebai et al., 2006; Sicilia et al., 2008).

3. Data Set and Methods

We followed the long-period ambient noise waveform inversion methods and workflow based on the scattering integral method (Chen et al., 2007; Shen et al., 2012; Zhang & Shen, 2010; Zhang et al., 2012; Zhao et al., 2005). This approach has been applied on a range of scales to several other regions including the western United States (Gao & Shen, 2012, 2014, 2015), the entire Eastern Hemisphere (Shen & Zhang, 2012), the Ontong Java Plateau (Covellone et al., 2015), and Eastern North America (Savage et al., 2017). Descriptions of the methods are outlined in those studies, so we include only a brief description here.

3.1. Ambient Noise Data sets

We gathered continuous records of ambient seismic noise from the Incorporated Research Institutions for Seismology Data Management Center for land-based broadband seismic stations located in Africa, the Middle East, and Southern Europe within the region defined by corners 40°S, 30°W and 45°N, 60°E (Figure 1). For all stations within Africa and the Middle East, we collected vertical component data from sensors with a low corner period of 120 s or greater. Due to the large number of sensors available in southern Europe, we were more selective with the quality of sensors, preferentially collecting data with a low corner period greater than 200 s. Data were split into synchronous daylong (24 hr) signals with an added buffer of 4 hr of overlap. In total, we obtained data from 851 broadband seismic stations throughout the region (Figure 1).

3.2. Extraction of EGF From Long-Period Ambient Noise

We extracted EGFs from the data using the approach detailed by Shen et al. (2012). Briefly, this method splits up ambient noise records into discrete time and frequency windows and normalizes the signal in order to better achieve the flat frequency spectrum of a diffuse wavefield (Shen et al., 2012). This method has been shown to improve the signal-to-noise ratio (SNR) of resulting EGFs, allowing longer-period signals to be acquired (e.g., Bensen et al., 2007; Shen et al., 2012). Following normalization, earthquakes with *Mw* 5.5+ were removed from the time series. The daylong records were cross-correlated for each station-station pair and were stacked to obtain EGFs for each set of stations. EGFs were then filtered into nine broad, overlapping frequency bands from 7 to 40, 25 to 55, 40 to 80, 60 to 100, 80 to 140, 110 to 180, 145 to 225, 180 to 260, and 220 to 340 s (see supporting information Figures S1–S3 for examples of long-period EGFs). From these, SNRs were calculated and EGF variances (σ) were obtained from monthly stacks of cross correlations. The estimates of error are later used when calculating phase delays relative to the synthetic waveforms. From the 851 broadband stations for which data were collected, 414 stations returned at least one quality EGF (SNR $>$ 5) for one or more of the nine period bands listed above, and 186 of these stations returned quality EGFs for one or more of the seven period bands greater than 40° (Figure 1; see supporting information Figure S4 for the distribution of station-station paths). EGFs from these 186 stations were convolved with the same Gaussian source time function (centered at 22.5 s, half-width 7.5 s) used to forward model the synthetics (described in the following section). Data that were brought into the inversion step, as discussed below, came from several permanent and temporary networks (network codes: AF, G, GE, GT, HL, II, IU, MN, PM, XA, XB, XS, XV, YF, YH, YL, ZK, and ZP).

3.3. Waveform Simulation

For each individual seismic station from which EGFs with SNR $>$ 5 were extracted in the frequency bands of interest, we model synthetic waveforms emanating from a virtual source at the station through a three-dimensional heterogeneous Earth structure (Zhang & Shen, 2010; Zhang et al., 2012). The synthetic wavefield is simulated using a spherical, collocated-grid finite difference waveform propagation method, which employs a region of complex-frequency shifted perfectly matched layers along the boundaries of the model domain to suppress artificial reflections off of the boundaries (Zhang et al., 2012; Zhang & Shen, 2010). The spherical grid is constructed with uniform spacing in latitude and longitude and nonuniform grid spacing in the depth direction (Zhang et al., 2012). The vertical grid spacing starts at one third of the horizontal grid spacing at the Earth's surface and increases with depth, so that it is roughly equal to the horizontal grid spacing at 100-km depth (Zhang et al., 2012).

A trade-off exists between the computational time required to model the full set of station-to-station synthetics while maintaining a dense enough finite difference grid to ensure accuracy of the shortest period waveforms (i.e., at least ~8 grid points per wavelength for body waves and ~15 grid points per wavelength for surface waves; see Zhang et al., 2012). For a lateral grid spacing of 0.2° in latitude and longitude, Rayleigh waveforms as low as 80 s are accurate, and for a lateral grid spacing of 0.1° in latitude and longitude, waveforms with periods as low as 40 s are accurate (e.g., Covellone et al., 2015; Gao & Shen, 2012, 2014). We utilized two high performance computing clusters located at the University of Rhode Island to model all synthetics and to invert the model using the EGFs extracted from ambient noise.

Our starting tomographic model was the CRUST 1.0 model (Laske et al., 2013) underlain by AK135 (Kennett et al., 1995) down to 1,100-km depth. The boundaries of the domain were set so that the first Fresnel zone of all station-station sensitivity kernels would lie within the domain. Our model domain was set to be several degrees larger than our initial station selection range, from 43°S, 34°W to 53°N, 68°E. We used a virtual source that is a single upward force, with a Gaussian source time function. During each model iterative step, synthetic waveforms were calculated by propagating a virtual source through the 3-D velocity model.

3.4. Waveform Inversion

For each iteration, the resulting synthetics from the waveform simulations were cross-correlated with the data from the EGFs to obtain a correlation coefficient and a phase delay. Those data with a correlation coefficient of 0.8 or greater were used to constrain the model during the iteration. As the three-dimensional model was refined during subsequent iterations, the synthetic waveforms fit to the data waveforms improved, and the number of data (convolved EGFs) that constrained the model increased (Figure 2).

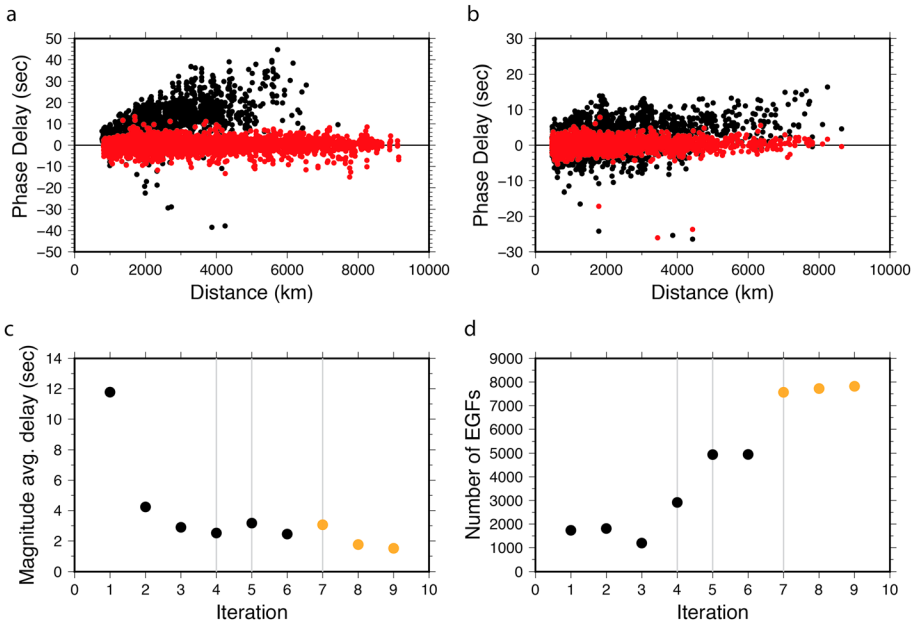

Figure 2. Phase delay reduction over the nine iterations of waveform inversion. (a) Phase delay measurements for all frequency bands (80–260 s) versus interstation distance for the initial model, CRUST1.0+AK135 (black dots), and after the final (ninth) iteration (red dots). (b) Same as in (a); however, the black dots correspond to the phase delay during the seventh iteration for the added higher-frequency bands (40–100 s). The red dots correspond to the final iteration for these two higher-frequency bands. (c) Magnitude of the average phase delay (d*t*) per iteration. The gray vertical lines mark the iterations where additional data were added to the inversion (see text for further explanation). Black dots are iterations 1–6, and orange dots are iterations 7–9 (denotes inclusion of higher-frequency EGF data). (d) Similar to (c), except that *y* axis denotes the number of EGFs used in each of the nine iterations. EGF = empirical Green's functions.

Both compressional and shear wave velocities contribute to Rayleigh wave propagation, particularly at shallow depth (Covellone et al., 2015; Gao & Shen, 2014; Savage et al., 2017). Our inversion was set up as a joint *Vp* and *Vs* inverse problem

$$\delta\mathbf{t}=\int\left[K_\alpha\left(\mathbf{m}_0,x\right)\Delta\mathbf{m}_\alpha+K_\beta\left(\mathbf{m}_0,x\right)\Delta\mathbf{m}_\beta\right]\mathrm{d}V$$

where $\delta\mathbf{t}$ is the phase delay between the synthetic and data (for cross correlations with correlation coefficients ≥0.8), $\Delta\mathbf{m}_\alpha$ and $\Delta\mathbf{m}_\beta$ were the perturbations (*Vp* and *Vs*, respectively) to the current 3-D Earth model at each block (*x*) within our model, and $K_\alpha(\mathbf{m}_0, x)$ and $K_\beta(\mathbf{m}_0, x)$ were the Rayleigh wave phase sensitivity kernels (*Vp* and *Vs*, respectively) calculated using the scattering-integral formulation (Zhao et al., 2005). Supporting information Figures S5 and S6 show examples of the sensitivity kernels to shear wave velocity perturbations and the spatial summation of all kernels used in the inversion. Density was not explicitly included in the inversion, though density is updated using an empirical *Vp*-density relation (Christensen & Mooney, 1995). Although the *Vp*-density relation is most applicable to crustal depths, the very minor *Vp* (and density) variations at upper mantle depths have a negligible effect on the *Vs* model (see supporting information Figure S7). During each iteration, new sensitivity kernels were calculated from the wave propagation through the 3-D velocity model.

Following the construction of sensitivity kernels, the inverse problem was solved for using a sparse, damped, least squares inversion method (Chen et al., 2007; Paige & Saunders, 1982; Zhao et al., 2005). The model was inverted using a number of smoothing and damping constraints, and a new model was selected so that the normalized chi-square misfit between data and synthetics was close to 1 (Gao & Shen, 2012; Montelli et al., 2004). The initial iterations of the model were oversmoothed and overdamped (see Table 1) with regard to this criterion; however, this was changed with subsequent iterations in accordance with Montelli et al. (2004) and Gao and Shen (2012).

Our inversion was initially run using a grid located at every 0.2° (~22 km); this allowed us to utilize longer-period EGF data (80+ s) to constrain broader and deeper structure first. For the first three iterations, a

Table 1
Information About Iteration Number, Grid Spacing of Waveform Simulations, Station Groupings (See Supporting Information), Cutoff Signal-to-Noise Ratio for EGFs Used to Constrain the Inversion and Smoothing and Damping Parameters

Iteration number[a]	Grid spacing (degrees)[b]	Station group[c]	Cutoff SNR	Smoothing	Damping
1–3	0.2	A	7	32	12
4	0.2	B	6	24	12
5	0.2	C	5	16	12
6	0.2	C	5	6	6
7	0.1	C	5	6	6
8	0.1	C	5	6	8
9	0.1	C	5	12	8

Note. EGF = empirical Green's functions; SNR = signal-to-noise ratio.
[a]For all iterations, phase delays were determined using a cross-correlation coefficient of 0.8 when correlating the EGFs (convolved with source time function) with synthetics. [b]Grid spacing and number of saved grids determines the inversion block size, as discussed in the main text. For iterations 1–6, every 5 grids were saved in the horizontal direction and every 1 grid was saved in the vertical direction. For iterations 7–9, every 10 grids were saved in the horizontal direction and every 2 grids were saved in the vertical direction. [c]Data from: Albuquerque Seismological Lab (1988, 1993), Athens (1997), Beck and Zandt (2005), Gao (2009), GEOFON data centre (1993), Institut De Physique Du Globe De Paris & Ecole Et Observatoire Des Sciences De La Terre De Strasbourg (1982), MedNet Project Partner Institutions (1990), National Observatory of Athens, Institute of Geodynamics, Silver (1997), Nyblade (2007), Penn State University (2004), Rondenay (2006), Scripps Institution of Oceanography (1986), Wiens and Nyblade (2005), Wysession et al. (2011).

subset of the EGFs, those with SNR $>$ 7, were utilized to constrain the overall regional structure more robustly. In subsequent iterations, we incorporated EGFs with SNR $>$ 6, then finally SNR $>$ 5. The first six iterations were completed using the coarser 0.2° grid. The inversion block size is decided by the number of saved spatial grids in each time snapshot of wave propagation; in the first few iterations, every five grids were saved in the horizontal direction and every one grid was saved in the vertical direction—producing a block size (and best possible resolution) of ~1° in the horizontal direction. Following the sixth iteration, the grid was resampled with a spacing of 0.1° (~11 km), moved onto a faster (1,200 cpu-core) cluster at the University of Rhode Island, and EGFs with periods of 40–340 s and SNR $>$ 5 were utilized to constrain the model. Due to data storage limitations, every 10 grids were saved in the horizontal direction and every 2 grids were saved in the vertical direction—once again producing a block size of ~1° in the horizontal direction. The model showed signs of convergence with the additional shorter period data (Figure 2) after three more iterations (seventh to ninth). Table 1 provides a summary of the grids and inversion parameters used.

3.5. Model Resolution

Despite the benefits of using full-waveform methods for tomographic inversions, the computational time required to generate a full suite of resolution tests would require the same amount of forward modeling and inversion time for each individual test case (e.g., Fichtner et al., 2009; Tape et al., 2007, 2010). As such, the tests we present demonstrate the recovery of an input synthetic model following a single iteration, using the sensitivity kernels that were calculated from the wave simulation and phase delays from the last model iteration (Figure 3 and supporting information Figures S7–S18). Although structure is improved upon in subsequent iterations, the resolution tests nevertheless provide guidance in interpretation of these results. We note that despite several differences in the data sets and methodology, (1) the overall upper mantle structure is similar to some other continental scale models (e.g., Fishwick, 2010; Pasyanos & Nyblade, 2007) and (2) small-scale upper mantle features in our models agree remarkably well with features imaged in regional tomographic studies (e.g., Adams et al., 2012, 2015; Bastow et al., 2008, 2005; Benoit, Nyblade, Owens, & Stuart, 2006, Benoit, Nyblade, & Pasyanos, 2006, Benoit, Nyblade, & VanDecar, 2006; Civiero et al., 2015; Gallacher et al., 2016; O'Donnell et al., 2013).

To assess the uncertainty in our final tomographic model due to the uneven spatial distribution of data in the region, we created a variety of resolution tests (Figure 3 and supporting information Figures S7–S18). In Figure 3, we show a checkerboard resolution test, consisting of 5° × 5° high (*Vs* +10% higher than AK135) and low (*Vs* −10% lower than AK135) shear velocity checkers extending through the entire depth range of the model. Our results suggest some slight northwest-southeast distortion of the recovered checkers in the sparsely instrumented portions of the model, which may indicate lateral smearing in parts of our final model. The checkerboard also indicates diminished ability to recover the amplitude of the anomalies at the shallowest upper mantle depth (~100 km), most notably beneath North Africa. The test also suggests that we are able to recover some of the input model at mantle transition zone (MTZ) depths (~400–450 km). Additional discussion of the methods and model resolution as well as several additional resolution tests can be found in the supporting information (e.g., Buehler & Shearer, 2016; Emry et al., 2011; Maceira et al., 2015; Montelli et al., 2006; Rhie & Romanowicz, 2004; Stehly et al., 2006; Zhou et al., 2011).

4. Results

We present isotropic shear wave speeds (*Vs*) in continental Africa (Figure 4 and supporting information Figures S19–S21). The best resolution in our model exists in North Africa, Central Africa, the East African Rift, and the Arabian Peninsula, and the results are sensitive to Earth structure down to MTZ depths (Figure 3 and supporting information Figures S7–S18). Although we invert for both shear and compressional wave speeds, Rayleigh wave sensitivities to the compressional wave speed are primarily located

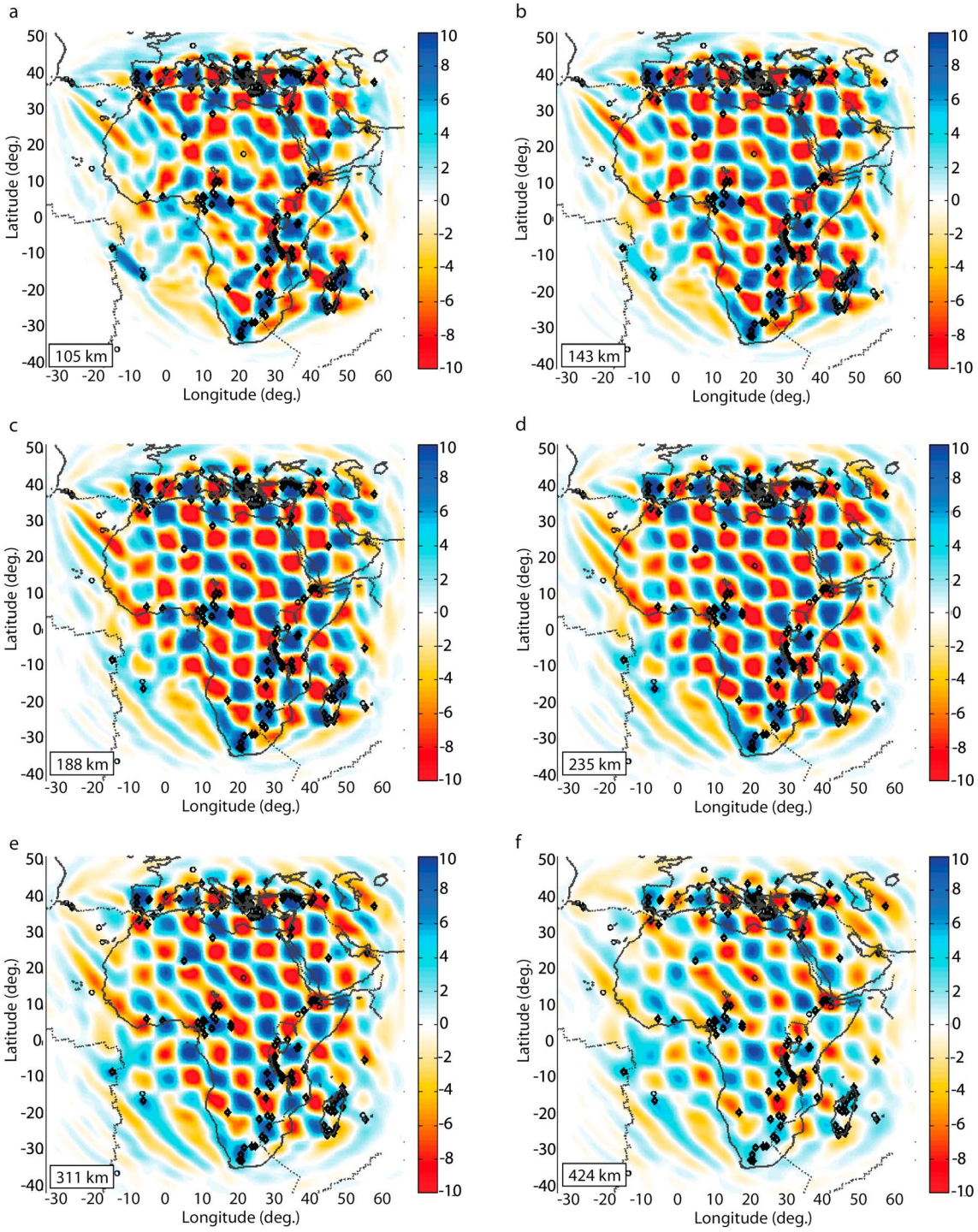

Figure 3. *Vs* checkerboard test. Plots show the estimated lateral resolution of the model domain through a checkerboard test with alternating fast (+10%) and slow (−10%) checkers at (a) 105 km, (b) 143 km, (c) 188 km, (d) 235 km, (e) 311 km, and (f) 424 km. Each checker is 5° × 5° square and is separated by the adjacent checker by 2° of average velocity (white). The checkers show the amount of anomaly recovered after one iteration, assuming the sensitivity kernels from iteration 9. The plots show that lateral resolution and anomaly amplitude are recovered well through the upper mantle with some ability to recover structure at MTZ depths.

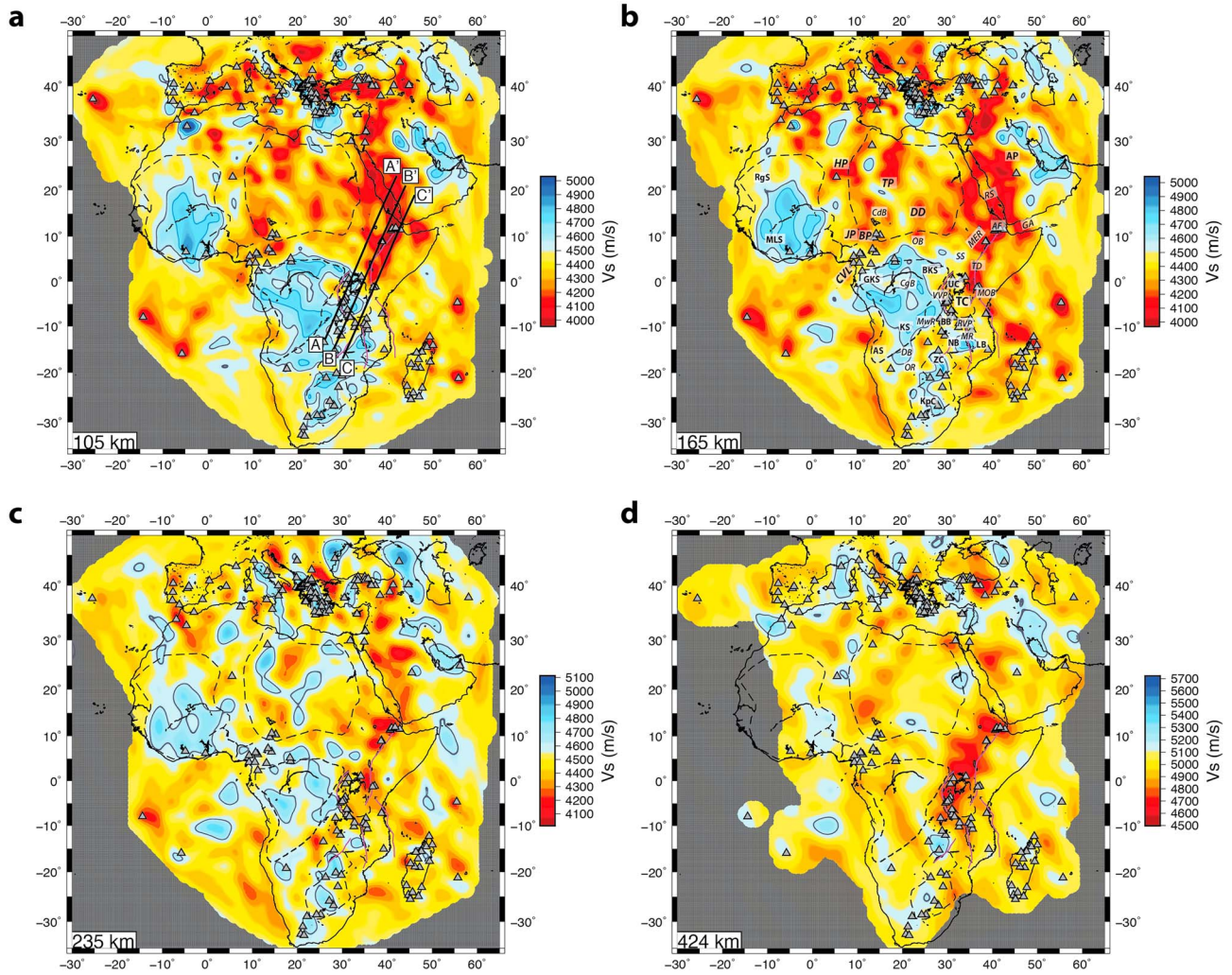

Figure 4. Isotropic *Vs* depth slices are shown as absolute velocity (m/s) at (a) 105 km, (b) 165 km, (c) 235 km, and (d) 424 km. The color bar is set to ±12% of AK135 global average Earth model (Kennett et al., 1995) at each depth. The model is masked by gray where it is not expected to have sensitivity to structure (see supporting information Figure S6). Gray triangles (same as red triangles in Figure 1) show seismic stations for which high-SNR EGFs contributed to the model. Black lines outline coast, lakes, and major rivers. In (a), thick black lines indicate cross-sectional lines corresponding to Figure 5. In (b), labels correspond to those in Figure 1. In all, gray contour lines indicate where shear velocities are 1.7% fast in comparison to the global average (as in Darbyshire et al., 2013). In (a) and (b), blue contour lines indicate where shear velocities are equal to 4.7 km/s; this velocity contour was suggested by Garber et al. (2018) to denote regions within cratons where eclogite and/or diamonds may be contributing to fast velocities at depths of ~120–150 km. Dashed black lines correspond to the boundaries of cratons and metacratons, and thin, purple lines show segments of the EARS, as in Figure 1.

at shallow depths, which are not greatly relevant to the discussion of structure within the upper mantle and MTZ within this paper (supporting information Figures S7 and S10).

In general, several low (shear) velocity regions are imaged in the upper mantle, and in some regions at the MTZ, beneath the EARS, the Cameroon Volcanic Line, the Angola (Bie) Dome, and North Africa (Figure 4). Profound differences in the average uppermost mantle *Vs* are observed between the northern and eastern segments of the EARS (*Vs* ~ 4.47 km/s at 100 km) and the southern and western segments of the EARS (*Vs* ~ 4.6 km/s at 100 km), due to the presence of thick cratonic structures located along the edges of the less developed southern and western sides of the EARS (Figure 5 and supporting information Figure S22). A comparison between our results and prior *Vs* models for several slow velocity anomalies throughout Africa is shown in Table 2, and an expanded table is provided in the supporting information.

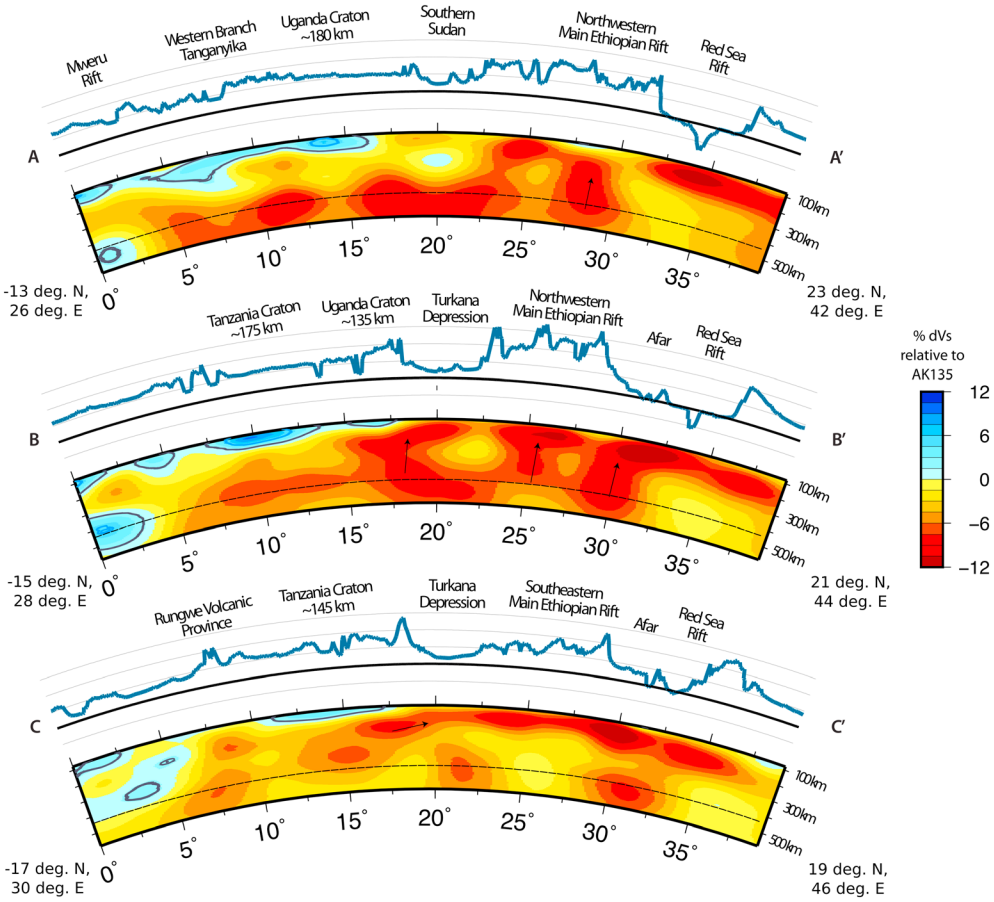

Figure 5. (a–c) Cross sections are plotted from southwest to northeast along the East African Rift System (corresponding to cross-section lines in Figure 4). Distance is shown in degrees, and depth is shown in kilometers. Velocities are relative to the AK135 global average Earth model (Kennett et al., 1995). The color scale ranges from 12% faster than AK135 (blue) to *Vs* 12% slower than AK135 (red). Thick gray contour lines are shown where *Vs* is 1.7 times greater than AK135 (Darbyshire et al., 2013), and thick light blue contour lines show where *Vs* is 5% greater than AK-135 (corresponding with 4.7 km/s velocities at ~120- to 150-km depths, as in Garber et al., 2018). The top of the mantle transition zone (410 km) is shown as a dashed line. For each cross section, the topography profile is provided above in thick blue lines. Here the thick black line denotes sea level and the thin gray lines denote intervals of 1 km.

In our results, we show several regions of thick, cratonic lithosphere. While lithospheric thickness is defined by different metrics, one common approach is to classify thickness as depth at which the model is not faster (or is some percentage faster) than a global average model (e.g., Darbyshire et al., 2013; Eaton et al., 2009). Archean cratonic lithosphere is highly depleted in iron, making it less dense, more rigid, and longer lived (Griffin et al., 2009). However, xenolith sample locations rarely correspond to regions with the highest observed seismic velocities (Garber et al., 2018; Griffin et al., 2009); recent petrological modeling suggests that very high *Vs* anomalies (>4.7 km/s) found in cratonic cores may also require some amount of eclogite (<20%) and diamond (2%) in the cratonic mantle lithosphere (Garber et al., 2018). To provide estimates of lithospheric thickness and possible compositional indicators, we show contour lines associated with a *Vs* ~1.7% faster than AK135 (Darbyshire et al., 2013) and associated with *Vs* = 4.7 km/s (or 5% faster than AK135 in cross-sectional lines; Garber et al., 2018). In each following results section, we highlight the details of our isotropic *Vs* model and provide a brief comparison between our models and prior work. A more detailed comparison between models for Africa, the Mediterranean, and the Middle East is included in the supporting information (Figure S23; Achauer & Masson, 2002; Ayadi et al., 2000; Benoit et al., 2003; Brazier et al., 2000; Bufford et al., 2012; Corbeau et al., 2014; Corchete, 2013; Dorbath et al., 1986; Fichtner et al., 2013; Fichtner & Villaseñor, 2015; Green et al., 1991; Hansen et al., 2006; Houser et al., 2008; Jakovlev et al.,

Table 2
Table Provides a Comparison of Absolute Shear Velocity for Several of the Main Hot Spot and Low-Velocity Anomalies Located Along the East African Rift System and Northern Africa

East African rift system velocity comparison									North Africa velocity comparison		
Low *Vs* anomaly (km/s) ~100-km depth	Red Sea, Saudi Arabia	Gulf of Aden	Afar	Main Ethiopian Rift	Turkana	Eastern Branch	Western Branch	Northern Malawi	Hoggar and Tibesti	Darfur	Cameroon Volcanic Line
This study (Emry et al.)	3.9–4.2	4.0–4.3	3.7–4.1	3.8–4.3	4.1–4.2	4.1–4.3	4.2–4.4	4.3–4.5	4.0–4.3	4.1–4.2	4.0–4.3
Nolet and Mueller (1982)	x	x	x	x	x	4.2	4.5	x	x	x	x
Ritsema and van Heijst (2000) (ref. PREM)	4.2–4.3	4.2–4.3	4.2–4.3	4.2–4.3	4.3–4.4	4.3–4.4	Not slow	Not slow	4.4	4.4	4.4
Pasyanos and Walter (2002) (upper mantle)	4.1–4.4	4.1–4.3	4.1–4.3	4.2–4.4	4.3–4.4	4.3–4.4	x	x	4.2–4.4	4.3–4.4	4.3–4.5
Weeraratne et al. (2003)	x	x	x	x	x	3.8	4.0	x	x	x	x
Sebai et al. (2006) (ref. PREM-SV, 80 km)	4.1–4.14	4.1–4.14	4.05	4.1–4.14	Not slow	Not slow	Not slow	Not slow	Not slow	Not slow	4.2–4.3
Dugda et al. (2007)	x	x	3.7–4.1	4.0–4.2	x	x	x	x	x	x	x
Pasyanos and Nyblade (2007) (ref. AK-135)	4.2–4.3	4.1–4.2	4.1–4.2	4.1–4.2	4.1–4.2	4.3–4.4	Not slow	Not slow	4.3–4.4	Not slow	4.3–4.4
Priestley et al. (2008) (ref. 4.412 km/s)	4.2–4.3	4.1–4.2	4.1	4.1–4.2	4.2–4.3	4.3–4.4	Not slow	Not slow	4.2–4.3	4.3–4.4	4.4–4.5
Sicilia et al. (2008) (ref. PREM-SV)	4.1–4.2	3.9–4.1	3.9–4.1	4.1–4.2	4.2–4.3	4.2–4.3	4.3	Not slow	4.2–4.3	4.2–4.3	3.9–4.1
Dugda et al. (2009)	x	x	x	x	x	4.0	x	x	x	x	x
Fishwick (2010) (ref. AK-135)	4.1–4.3	4.0–4.1	4.0–4.1	4.1–4.2	4.1–4.3	4.2–4.3	Not slow	Not slow	4.2–4.3	4.2–4.3	4.1–4.2
Tokam et al. (2010; 80-km depth)	x	x	x	x	x	x	x	x	x	x	4.3–4.4
Chang and van der Lee (2011)	4.1–4.3	4.1–4.2	4.1	4.1–4.2	4.3–4.5	x	x	x	x	x	x
Adams et al. (2012)	x	x	x	x	x	4.25–4.35	4.2–4.3	4.25–4.35	x	x	x
O'Donnell et al. (2013)	x	x	x	x	x	4.3	4.4	4.2	x	x	x
Schaeffer and Lebedev (2013) (ref. 4.38 km/s)	4.1–4.2	4.1–4.2	4.1–4.2	4.1–4.2	4.1–4.3	4.2–4.3	Not slow	Not slow	4.15–4.2	4.2	4.2
Adams et al. (2015)	x	x	x	x	x	x	x	x	x	x	4.15–4.2
Gallacher et al. (2016)	x	3.9–4.0	3.85–3.95	3.8–4.0	x	x	x	x	x	x	x
Yao et al. (2017)	4.0–4.2	x	x	x	x	x	x	x	x	x	x

Note. This comparison includes models that are global, continental, and regional in scale with resolution predominantly within the upper mantle at 90- to 110-km depth (unless otherwise stated in column 1). An "x" denotes that the model does not have information for the region. Additional *Vp*, d*Vp*, and d*Vs* results are provided in the supporting information.

2013; Khoza et al., 2013; Korostelev et al., 2015, 2016; Leseane et al., 2015; Mulibo & Nyblade, 2013b; Nita et al., 2016; Nyblade, 2011; Nyblade & Brazier, 2002; Nyblade et al., 2000; Reed, Gao, et al., 2016; Reed, Liu, et al., 2016; Ritsema et al., 2011, 1998; Slack et al., 1994; Sun et al., 2017; Yu et al., 2015).

4.1. The Congo Craton and Angola Dome

Our model results show separate high wave speed anomalies at upper mantle depths beneath the Congo Craton, with highest velocities (*Vs* +5–10% of AK135 and ~4,700–4,850 m/s) located near the Archean aged Bomu-Kibalan Shield in the north-northeast and the Kasai and Angolan Shields in the south-southeast (Figure 6; e.g., Begg et al., 2009). Less pronounced high wave speed anomalies (*Vs* +2–5% of AK135) are located in the northwest, near the position of the Gabon-Kamerun Shield (e.g., Begg et al., 2009). Our model continues to show separation between high-velocity blocks to ~200- to 250-km depth, with the deepest, highest-velocity cratonic roots in the north, east, and south-southwest. While the locations and depth extents differ, a separation between high velocities was imaged in a few earlier studies (Fishwick, 2010; Pasyanos & Nyblade, 2007; Raveloson et al., 2015). At the southwestern edge of the Congo region, beneath the Angola dome, a prominent low-velocity anomaly can be seen at depths of 100–300 km; this feature has only been somewhat resolved in a few prior studies (Colli et al., 2013; Fishwick, 2010; Schaeffer & Lebedev, 2013). Results from greater depths give no indication for a deep continuation of this low-velocity feature,

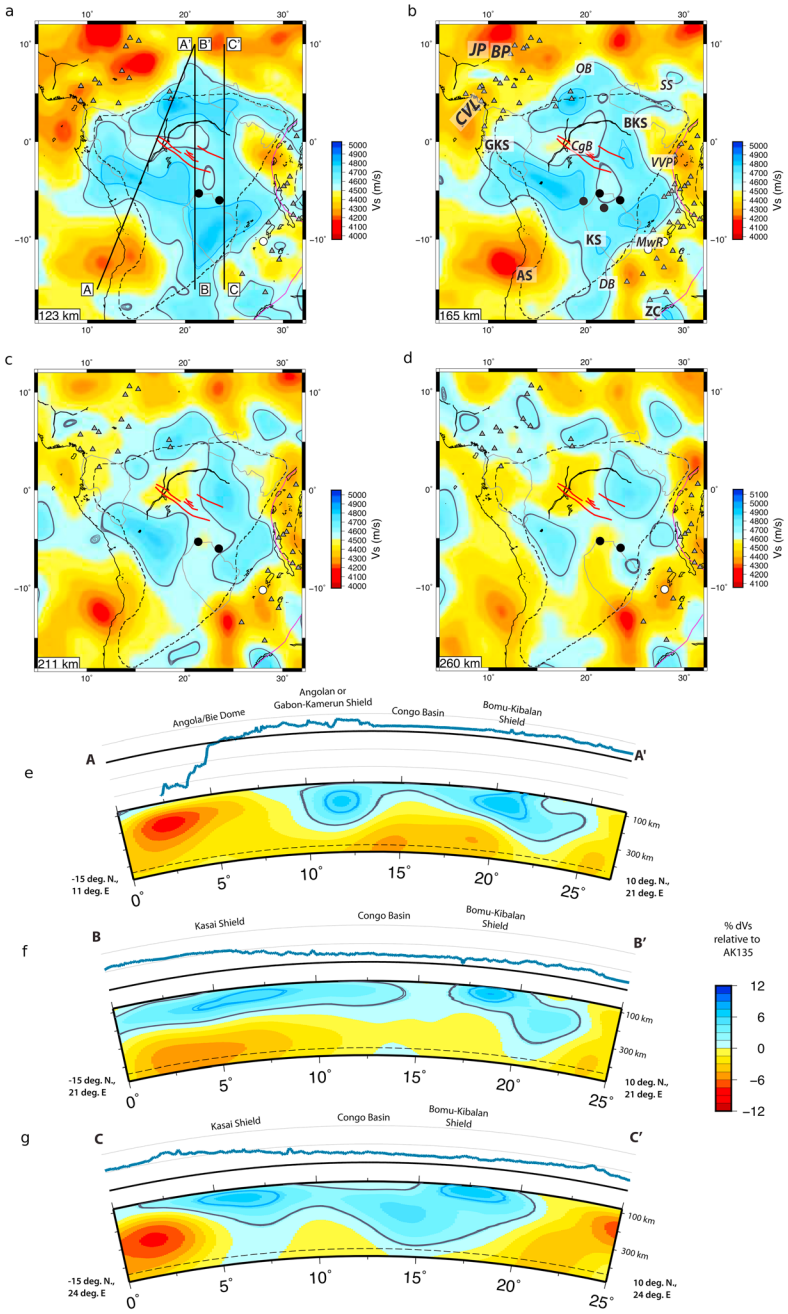

Figure 6. Upper mantle beneath the Congo Craton. The depth slices show the absolute *Vs* (m/s) for our model results beneath the Congo Craton region with (a) 123-km depth, (b) 165 km, (c) 211 km, and (d) 260 km. The proposed boundaries of one large Congo Craton and the western edge of the neighboring Tanzania Craton are outlined by dashed black lines, and thin, purple lines show segments of the East African Rift System, as in Figure 1. Archean shields exposed at the surface within the Congo region are outlined by light gray lines (from Begg et al., 2009; Raveloson et al., 2015). The red lines in the center of the Congo region are subbasin fault locations discussed in Kadima et al. (2011). Gray triangles denote seismic stations with data used in the inversion. Black circles denote locations where diamonds suggest thick lithosphere (~200 km), and white circles denote locations where they suggest thinner lithosphere (~160 km; Batumike et al., 2009). Cross-section lines plotted on (a) are shown for (e) A-A′ from the Angola Dome to the Central African Shear Zone, for (f) B-B′ from the southern Kasai Shield to the Central African Shear Zone, and for (g) C-C′ from the Mweru Rift to the Central African Shear Zone. As in Figures 4 and 5, thick gray contour lines denote where *Vs* is 1.7 times greater than AK135 (Darbyshire et al., 2013) and thick, light-blue contour lines show where *Vs* is 5% greater than AK-135 (in cross section) or where *Vs* is 4.7 km/s in (a) and (b; Garber et al., 2018). The top of the mantle transition zone (410 km) is shown as a dashed line. For each cross section, the topography profile is provided above in thick blue lines; the thick black line denotes sea level, and the thin gray lines denote intervals of 1 km.

although at those depths, the resolution of our model diminishes (Figure 3 and supporting information Figures S6, S8, and S9).

4.2. The EARS and the Arabian Peninsula

In the northernmost region of our model, beneath the Red Sea Rift and the Western Arabian Peninsula, low velocities were imaged down to ~200- to 250-km depth (Figures 4 and 7). Below that, low velocities were focused beneath the western Arabian Peninsula, with a low-velocity anomaly near MTZ depths beneath northwestern Saudi Arabia; this is similar to but offset slightly from earlier results from Chang and van der Lee (2011). Our spatial resolution of this region is good down to MTZ depths (Figure 3 and supporting information Figures S6, S8, S9, S16, and S17). On the southern edge of the Arabian Peninsula, beneath the Gulf of Aden (between Northern Somalia and western Yemen), we image a prominent low-velocity anomaly at shallow upper mantle depths. At deeper depths, the low velocities appear to shift west, toward the Afar region (Figures 4 and 7); again, our resolution tests suggest that the pattern is resolvable. (Figure 3 and supporting information Figures S6, S8, and S9).

The upper mantle beneath Afar and the Main Ethiopian Rift regions is marked by pronounced low shear wave velocities (~4,000 m/s), as low as ~10–12% less than AK135, similar to several prior studies (Figure 7 and Table 2; e.g., Bastow et al., 2008; Chang & van der Lee, 2011; Dugda et al., 2007; Fishwick, 2010; Gallacher et al., 2016; Ritsema & van Heijst, 2000; Sebai et al., 2006; Sicilia et al., 2008). At middle to deep upper mantle depths (>150 km), this region of low velocity is located beneath the northwestern side of the Main Ethiopian Rift and Afar. The lowest velocities within this region appear to be located within two, possibly distinct, regions (~12–15°N, 35–40°E; one at ~8–10°N, 34–36°E), similar to some earlier tomographic results (Bastow et al., 2008; Benoit, Nyblade, Owens, & Stuart, 2006, Benoit, Nyblade, & VanDecar, 2006; Civiero et al., 2015, 2016). At MTZ depths, low-velocity features are broadly located through the whole region, extending south along the EARS; however, we caution that if distinct, closely spaced (<500 km) low-velocity anomalies existed at MTZ depths, they could appear to be broad, connected features due to increased lateral smearing at MTZ depths (supporting information Figures S16–S18).

Beneath the Turkana Depression, at shallow upper mantle depths (100–150 km), our results suggest low shear wave velocities in the east, directly beneath Lake Turkana, but nearly average upper mantle velocities to the west beneath South Sudan. In our model, the upper mantle low shear velocity beneath Turkana (4.0–4.2 km/s, 105 km) is similar to the low Sn velocities (4.1–4.2 km/s, uppermost mantle) found previously by Benoit, Nyblade, and Pasyanos (2006); however, in our model, the slowest velocities are located further east and centered beneath Lake Turkana. Conversely, at middle upper mantle depths (~150- to 300-km depth), our results suggest a high-velocity feature (~+3%) in the west and nearly average upper mantle velocities in the east, beneath the Turkana Depression; this feature appears to be well resolved and not strongly susceptible to lateral smearing (Figure 3 and supporting information Figures S8 and S14). This entire region appears to be underlain by a broad, prominent low-velocity feature at MTZ depths; but again, it is difficult to determine whether distinct features at the MTZ could be individually resolved.

To the south, the EARS branches around the Tanzania Craton, along the Eastern and Western Branches (Figures 4 and 5). Our results suggest that the Tanzania craton is thinner in comparison to the other African cratons and is asymmetrical, with the western side thicker than the eastern side (120–145 km in the east and ~175 km in the west). The asymmetry and thickness estimates are similar to several other surface wave studies (Adams et al., 2012; Fishwick, 2010; O'Donnell et al., 2013; Weeraratne et al., 2003), but they differ from a few prior estimates of thicker Tanzania Craton lithosphere (Priestley et al., 2008; Ritsema & van Heijst, 2000).

In the region surrounding the Tanzania Craton, low velocities are imaged most prominently at shallow upper mantle depths in the northeast, beneath the northern side of the Eastern Branch. This low-velocity feature appears to shift south at mid-upper mantle depths (Figure 4 and supporting information Figure S22). At uppermost mantle depths beneath the Western Branch, the shear wave velocity is predominantly high, with one low-velocity anomaly near the Virunga volcanic field. The anomaly beneath Virunga becomes less prominent at mid-upper mantle depths but may spread south beneath the amagmatic Tangyanika Rift (O'Donnell et al., 2016) and the Mweru Rift region. This pattern at shallow depth resembles some earlier tomographic results (Adams et al., 2012; Grijalva et al., 2018; O'Donnell et al., 2013,

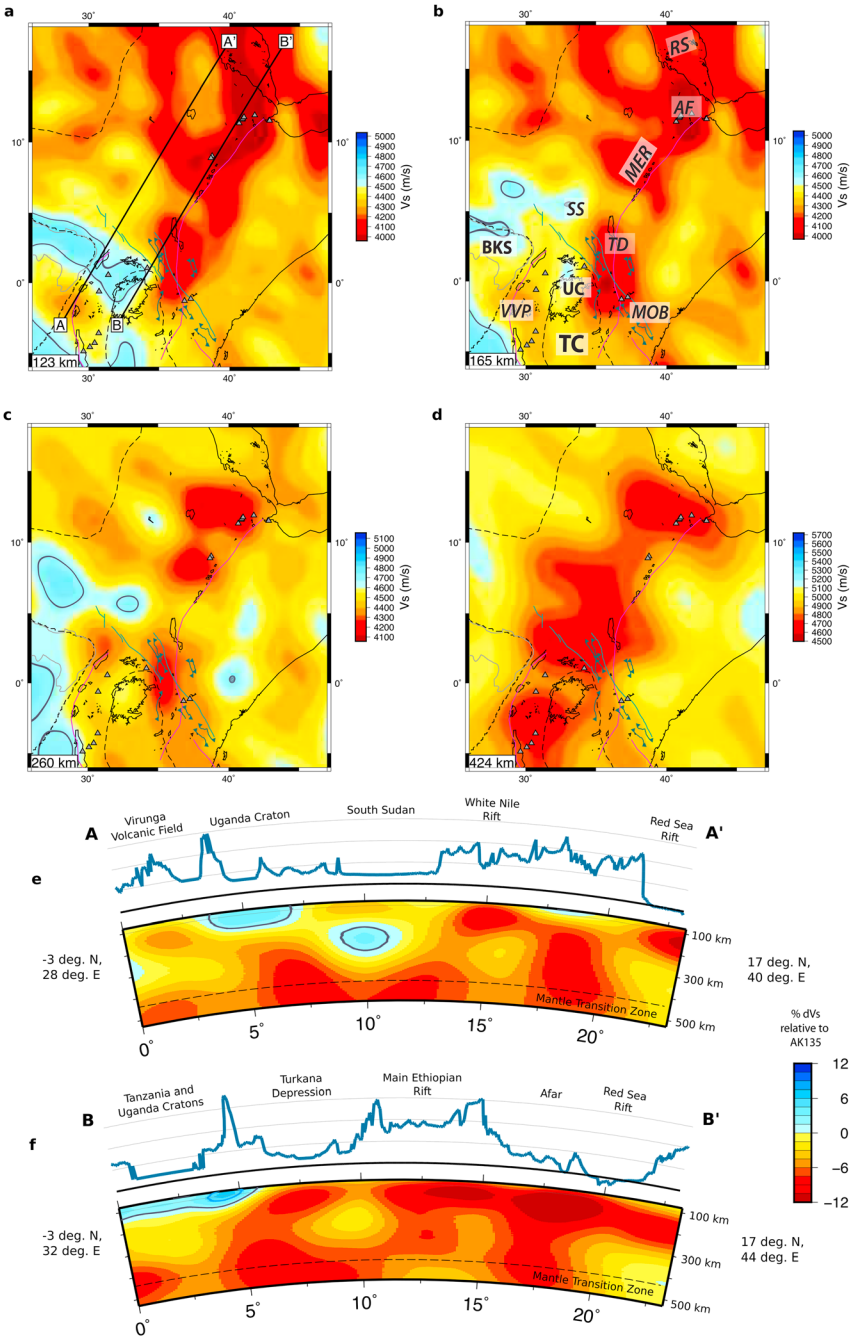

Figure 7. Upper mantle and mantle transition zone beneath the Turkana Depression. The above depth slices show the predicted absolute *Vs* (m/s) for our model results beneath the Turkana Depression and the Ethiopian and East African Plateaus at (a) 123-km depth, (b) 165 km, (c) 260 km, and (d) 424 km. The proposed boundaries of one large Congo Craton and the neighboring Tanzania Craton are outlined by dashed black lines, and thin, purple lines show segments of the East African Rift System, as in Figure 1. Archean shields exposed at the surface within the Congo region are outlined by light gray lines (from Begg et al., 2009; Raveloson et al., 2015). Gray triangles denote seismic stations with data used in the inversion. The solid green-blue lines show strike-slip faults and shear zones, including the Aswa-Nandi Shear Zone, and the green-blue thrust lines show thrust lines show several of the mapped thrust faults running parallel to the trend of the Anza Graben and Aswa shear zone (from Chorowicz, 2005; Saalmann et al., 2016). Cross sections from (a) are shown for (e) A-A′ from Virunga Volcanic Field to the Red Sea and for (f) B-B′ from the Tanzania Craton to Afar and the Red Sea. As in Figures 4 and 5, thick gray contour lines denote where *Vs* is 1.7 times greater than AK135 (Darbyshire et al., 2013) and in the cross sections, thick, light-blue contour lines show where *Vs* is 5% greater than AK-135 (Garber et al., 2018). The top of the mantle transition zone (410 km) is shown as a dashed line. For each cross section, the topography profile is provided above in thick blue lines; the thick black line denotes sea level, and the thin gray lines denote intervals of 1 km.

2016; Weeraratne et al., 2003). Beneath the entire region, a low-velocity anomaly is imaged near MTZ depths; in our model, this is most prominent beneath the Western Branch, suggesting that the low-velocity feature might gradually shift toward the southwest (Figure 5).

In the southwestern EARS, we image a clear separation between the cratonic features in southernmost Africa and the Congo region (Figure 4 and supporting information Figures S20 and S21). South of the Mweru Rift, but north of Okavango, we image a low-velocity feature at upper mantle depths. It is not clear whether this feature continues all the way downward to the MTZ, as it is possible that the low-velocity anomaly is vertically smeared. To the east, beneath the southern arm of the EARS, we detect slight, low-velocity anomalies at shallow upper mantle depths beneath the Rungwe Volcanic Province. Further to the south along the Malawi and Luangwa Rift, we detect a prominent high wave speed anomaly (+5–7%) beneath the southern Lake Malawi region at upper mantle depths (~100–200 km), as imaged by Sarafian et al. (2018) and Adams et al. (2018). This portion of our model domain is well covered due to seismic data collected throughout Madagascar (e.g., Andriampenomanana et al., 2017; Pratt et al., 2017).

Overall, the most prominent upper mantle low-velocity features are broadly located throughout the Main Ethiopian Rift and Eastern Branch of the EARS, while at upper mantle depths low velocities are more localized in distinct regions of the western and southern EARS. At MTZ depths, low velocities are imaged along much of the EARS, most prominently beneath the South Sudan and Turkana Depression regions. Our resolution tests suggest that these features are robustly distinct from the MTZ low velocity beneath the northwestern Arabian Peninsula, but at smaller lateral distances (~500 km or less), anomalies are not as distinctly resolved at MTZ depths as they are at shallow to mid-upper mantle depths (supporting information Figures S16–S18).

4.3. North Africa and the Cameroon Volcanic Line

Throughout northern Africa, we observe several regions of low wave speed (Figure 8 and supporting information Figure S24), similar to results from Fishwick (2010). At slightly deeper depths, in the mid-upper mantle beneath the Sahara, our results suggest several high-velocity structures; this is somewhat similar to earlier studies, although located at slightly different positions (Liégeois et al., 2013; Pasyanos & Nyblade, 2007; Sebai et al., 2006; Sicilia et al., 2008). Due to difficulty resolving structure in the shallow upper mantle beneath the Sahara Desert (few seismic stations), it is not clear whether these high-velocity structures also exist at shallow upper mantle depths or whether they are truly disconnected from structure above (Figure 3 and supporting information Figures S8 and S9). At deeper depths, on the southwestern side of the Sahara Metacraton region, a low-velocity anomaly is imaged beneath the western side of the Chad Basin and eastern Niger, possibly extending to the MTZ, although vertical smearing may influence that result (Figures 1, 8, and supporting information Figure S15). This deep upper mantle or MTZ feature is particularly noteworthy, because at shallow depths it appears to connect to the northern extent of the Cameroon Volcanic Line (Adams et al., 2015).

5. Interpretation

5.1. Cratonic Structure in Africa

5.1.1. The Congo Craton

Our results suggest separation between high wave speed anomalies beneath the northern and southern Congo Craton (Figure 6 and supporting information Figures S12 and S13), and we suggest that this indicates that the Congo craton is composed of smaller high-velocity blocks that were sutured during earlier orogenic events. The region between the cratonic fragments has thin or low-velocity lithosphere (~100–150 km), compared to the cratonic high-velocity blocks with thicknesses of ~200–250 km, where thickness is defined as 1.7% faster than AK135 (e.g., Darbyshire et al., 2013; Figure 6). The location of the cratonic fragments roughly coincides with Archean-aged outcrops at the surface; the highest velocities are horizontally offset from surface exposures at deeper depths, although this offset may partly be due to smearing of structure from neighboring slow anomalies beneath the Damara Belt and Western Branch (Begg et al., 2009). Despite this, our resolution tests reinforce that (1) we have coverage of this region and resolution is best at mid-upper mantle depths and (2) we are able to distinguish between one, large cratonic block and individual blocks (Figure 6 and supporting information Figures S12 and S13). Our results also show high velocities (>4.7 km/s) that were recently proposed by Garber et al. (2018) to be due to compositional variations within cratonic lithosphere. However, because lateral and

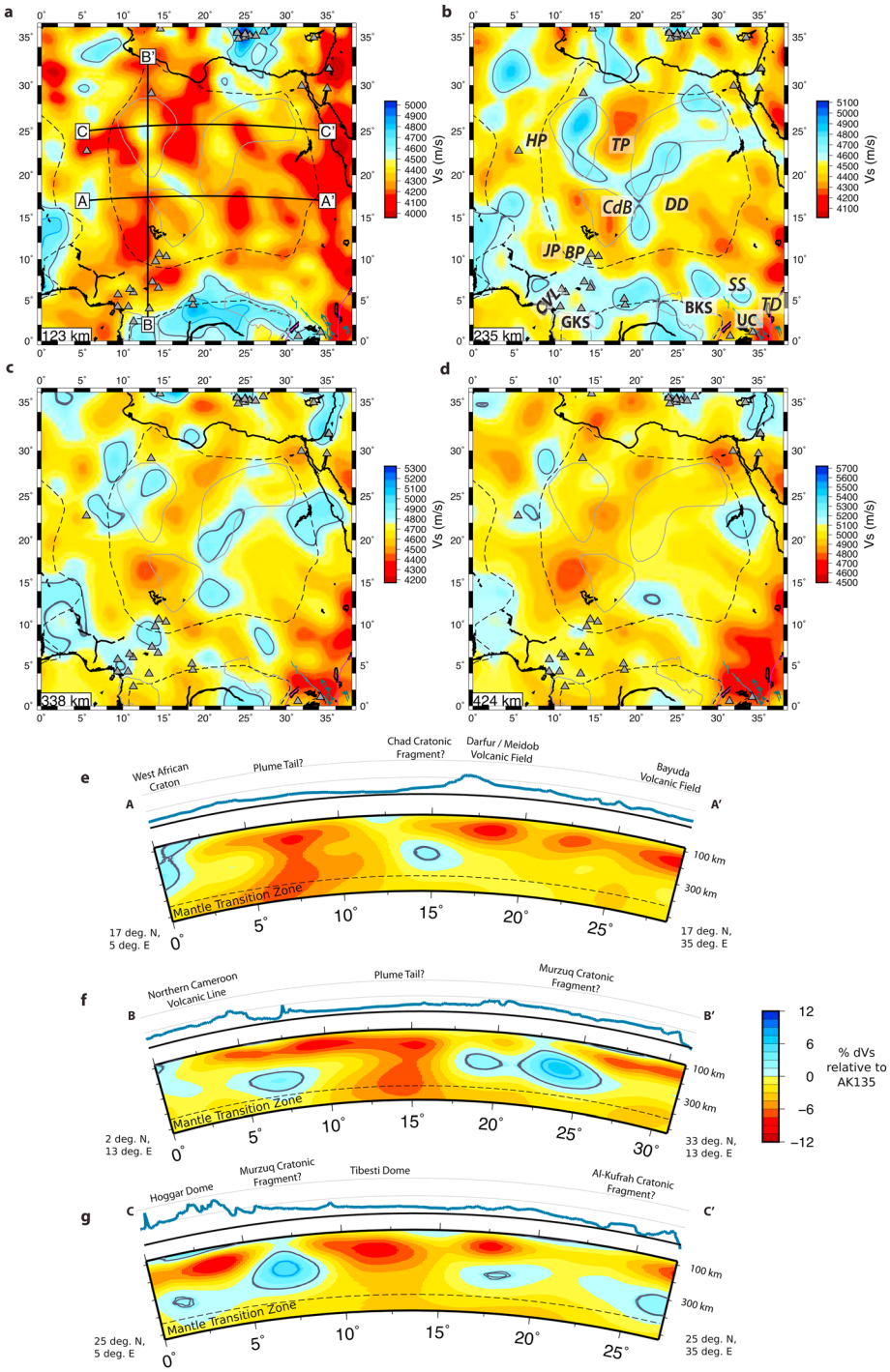

Figure 8. Upper Mantle beneath North Africa. *Vs* (m/s) is plotted at (a) 123-km depth, (b) 235 km, (c) 338 km, and (d) 424 km. The larger Congo Craton and the Sahara Metacraton are outlined by dashed black lines, and thin, purple lines show segments of the East African Rift System, as in Figure 1. Archean shields exposed at the surface within the Congo region and the proposed boundaries of the Chad (south), Murzuq (northwest), and Al-Kufrah (northeast) cratonic fragments within the larger Sahara Metacraton are outlined by light gray lines (from Begg et al., 2009; Liégeois et al., 2013; Pasyanos & Nyblade, 2007; Raveloson et al., 2015). Gray triangles denote seismic stations with data used in the inversion. The solid green-blue lines show strike-slip faults and shear zones, and the green-blue thrust lines show several of the mapped thrust faults running parallel to the trend of the Anza Graben and Aswa shear zone (from Chorowicz, 2005; Saalmann et al., 2016). Cross sections from (a) are shown for (e) A-A′ from the West African Craton to the Bayuda Volcanic Field in northern Sudan, for (f) B-B′ from the Cameroon Volcanic Line to the Mediterranean Sea, and for (g) C-C′ from the Hoggar Plateau to the Red Sea. As in Figures 4 and 5, thick gray contour lines denote where *Vs* is 1.7 times greater than AK135 (Darbyshire et al., 2013) and thick, light-blue contour lines show where *Vs* is 5% greater than AK-135 (in cross section) or where *Vs* is 4.7 km/s in (a; Garber et al., 2018). The top of the mantle transition zone (410 km) is shown as a dashed line. For each cross section, the topography profile is provided above in thick blue lines; the thick black line denotes sea level, and the thin gray lines denote intervals of 1 km.

vertical smearing is apparent from the resolution tests, we recommend against interpreting the fast and slightly fast velocities as evidence for lithospheric layering here (e.g., Darbyshire et al., 2013; Fischer et al., 2010; Yuan & Romanowicz, 2010). If a thick cratonic root is present along the Western Branch of the EARS, as the cross sections in Figure 6 suggest, it could influence patterns of upper mantle flow, rifting, and volcanism along the EARS; we will discuss this in a later section.

Many previously proposed mechanisms for subsidence at the Congo Basin assume a single, thick cratonic root beneath the basin (e.g., Buiter et al., 2012; Crosby et al., 2010; Downey & Gurnis, 2009; Hartley & Allen, 1994). Rather, our results are more compatible with the interpretation that separate, thick cratonic fragments were sutured during the Proterozoic and have undergone subsequent deformation (Daly et al., 1991; de Wit et al., 2008; Kadima et al., 2011; Pasyanos & Nyblade, 2007; Raveloson et al., 2015). In this scenario, the initial filling of the sedimentary basin results from rift-related subsidence and might have been followed by more recent subsidence due to sedimentation from adjacent uplifts (Buiter et al., 2012; Burke & Gunnell, 2008).

5.1.2. The Sahara Metacraton

Cratonic blocks within the larger Sahara Metacraton in northern Africa, the Murzuq, Chad, and Al-Kufrah (Uweinat) blocks have been previously proposed (e.g., Fezaa et al., 2010; Liégeois et al., 2013; Pasyanos & Nyblade, 2007). Our results in this region show high seismic shear velocities at mid-upper mantle depth (~250 km) that are coincident with previously proposed cratonic blocks, with the exception of the Chad cratonic block (Figure 8 and supporting information Figure S24; Liégeois et al., 2013). These high velocity features are subdued at shallow upper mantle depths (~100 km), possibly due to lateral smearing from adjacent low-velocity regions beneath the Hoggar, Tibesti, and Darfur Domes.

On the southeastern side of the Sahara Metacraton, in South Sudan, west of the Turkana Depression, a high wave speed feature is similarly imaged at mid-upper mantle depths but not at shallow depths (Figures 7 and 8). This feature strikes parallel to the Bomu-Kibalan cratonic fragment, and they may be connected. Our resolution tests suggest that if the feature in South Sudan was continuous from mid-upper mantle depths to the crust, we would be able to resolve it as a high-velocity structure that is continuous in depth, regardless of low velocities adjacent to it at shallow depth (supporting information Figures S8, S9, and S14). A common explanation for these patterns is not required, but we note that seismic tomography from Madagascar and Antarctica shows similar disconnected, high-velocity structures at mid-upper mantle depths (Shen et al., 2018; Wysession et al., 2017). Both the Sahara Metacraton and the Turkana Depression have experienced deformation and metasomatism during the Pan-African Orogeny (e.g., Abdelsalam et al., 2002, 2011; Guirard et al., 2000; Katumwehe et al., 2015; McGregor, 2015). We propose two possible explanations for these mid-upper mantle high velocities.

The first possibility is that high wave speed mid-upper mantle anomalies represent continental lithosphere that was thrust downward during one of the Pan-African collisional events but did not sink completely (e.g., Canil, 2004; Hirth et al., 2000; Lee et al., 2011; Shapiro et al., 1999; Tang et al., 2013). Regions of midlithospheric low-velocity anomalies have been observed in many regions around the world (see Karato et al., 2015; Rader et al., 2015; Selway et al., 2015), and one proposed mechanism is stacking of lithosphere during subduction, which in turn could explain the low velocities, either through variations in lithospheric anisotropy (e.g., Sodoudi et al., 2013; Wirth & Long, 2014; Yuan & Romanowicz, 2010) or through metasomatism between stacked slabs (Hopper & Fischer, 2015). Prior work from the eastern United States, using the methods employed in our paper, similarly imaged shallow lithospheric low velocities (Savage et al., 2017). Alternatively, this high-velocity overlain by low or average velocities could also be associated with some type of destabilized lithospheric root or delamination, as has been proposed for other tectonic settings (e.g., Göğüş et al., 2017; Shen et al., 2018; van Wijk et al., 2010; West et al., 2009). Such a mechanism would be expected to affect mantle flow (Shen et al., 2018; West et al., 2009), whereas for a stacked slabs scenario, the pattern may be stable, although prior metasomatism of the lithosphere may also enable subsequent destabilization (e.g., Snyder et al., 2017; van Wijk et al., 2010; Wang et al., 2015).

5.1.3. The Tanzania Craton

As mentioned, the Tanzania Craton is thicker (~175 km) in the west (Figure 5b) than in the east (~145 km; Figure 5c); at its very thinnest, it is ~110–120 km in the far eastern side, where it is adjacent to slow anomalies along the Eastern Branch. Similar to the cratonic blocks beneath Congo, the Tanzania lithosphere has notably high *Vs*. The asymmetry of the Tanzania Craton agrees with prior work proposing that the craton may be

thermally eroded along the Eastern Branch (e.g., Ebinger et al., 1997; Weeraratne et al., 2003); thermal erosion has also been suggested for other cratonic regions, including the North China and Wyoming Cratons (e.g., Dave & Li, 2016; Gao et al., 2008; Lee et al., 2011; Xu, 2001; Zhang et al., 2014). Geodynamic models suggest that prior cratonic root metasomatism enables thermal erosion to take place (e.g., Snyder et al., 2017; van Wijk et al., 2010; Wang et al., 2015), and we note that this region coincides with earlier Pan-African collision and prior alteration (Collins & Piesarevsky, 2005; Koornneef et al., 2009; Porada, 1989; Rino et al., 2008). At the same time, our present-day tomographic images cannot reveal whether the cratonic root asymmetry is due to recent thermal erosion or earlier tectonic events.

5.1.4. The Niassa Cratonic Fragment

In the southern EARS, beneath the southern Malawi Rift (Figures 1, 4, and supporting information Figures S19–S21), a prominent high-velocity feature is imaged in the upper mantle. This structure is located between the proposed Niassa and Lurio Archean nuclei within the Southern Irumide and Lurio Belts (Andreoli, 1984; Begg et al., 2009). This high-velocity structure also appears to coincide with a cratonic fragment recently imaged by magnetotellurics and regional seismic tomography (Adams et al., 2018; Sarafian et al., 2018). Because these fragments are small, we propose that the high-velocity feature we image is either the same Niassa craton identified by Sarafian et al. (2018) and Adams et al. (2018) or is a combined structure including both the Niassa and nearby Lurio Cratons. This region is unique, because it lies directly south of the Rungwe Volcanic Province (Accardo et al., 2017), suggesting that a cratonic root could be inhibiting volcanism on the southern end of the Malawi Rift.

5.2. Rifting and Volcanic Processes

Buoyant mantle plumes have been proposed to deflect around rigid structures and be channeled along regions of thinner lithosphere (Ebinger & Sleep, 1998). In the next sections, we discuss the possibility of plumes in the EARS, apparent influence of lithospheric topography, and what seismic velocities reveal about mantle temperature and melt beneath hot spots around Africa.

5.2.1. A Picture of Mantle Plumes

The prominent "African Superplume" has been seismically imaged as one, low-velocity anomaly, rising from the base of the mantle below the south Atlantic, flowing toward the EARS, and stretching through the upper mantle along the rift system (e.g., Hansen et al., 2012; Ritsema et al., 1999; Simmons et al., 2010, 2012). Our results are somewhat similar, in that we image an overall shift of low-velocity material toward the west-southwest at deeper depths. However, our results suggest a complex distribution of low velocities in the upper mantle, one that is not laterally continuous along the EARS (Figures 4 and 5). Instead, we propose that the discontinuous distribution of low velocities within the upper mantle is better explained by a set of secondary plumes that rise vertically from MTZ depths (Figure 5). At shallower depths, where upwellings encounter rigid lithosphere, the rising material may shift laterally toward regions of thinner lithosphere, as has been proposed at the Ethiopian Plateau and Main Ethiopian Rift (Bastow et al., 2008; Benoit, Nyblade, & VanDecar, 2006). The source for these secondary plumes could be a deeper ponded plume structure, as has been proposed in several prior studies of volcanic regions, including East Africa (e.g., Bastow et al., 2008; Cao et al., 2011; Christensen & Yuen, 1985; Civiero et al., 2015; French & Romanowicz, 2015; Furman et al., 2006; Huerta et al., 2009; Kieffer et al., 2004; Saki et al., 2015; Tosi & Yuen, 2011; Vinnik et al., 1997).

As shown in Figure 5, our results near MTZ depths do appear to be a continuous region of low velocity; but there is a limit to our ability to distinguish distinct plumes. If, as suggested by Chang and van der Lee (2011), three distinct upper mantle plume stems existed beneath East Africa and the Arabian Peninsula, our resolution tests suggest that they would be individually resolved (supporting information Figures S16 and S17). However, if multiple plume stems were located closer, they would smear together at MTZ depths (supporting information Figure S18; e.g., Civiero et al., 2015, 2016). At upper mantle depths (shallower than ~300 km), our resolution tests suggest that, despite a minor amount of lateral smearing, we are able to distinguish between a laterally continuous structure and distinct vertical features, such as a plume tail. We have confidence in our ability to resolve closely spaced upper mantle structures, as long as the separation between the features is ~500 km (~5°) or larger and the width of any such upwelling is ~200–300 km (supporting information Figure S18). Therefore, while we cannot distinguish between one large and several, small, closely spaced features at MTZ depths, we can reasonably expect to resolve distinct features at upper mantle depths, as long as ~500 km of separation exists.

The apparently distinct low-velocity features at upper mantle depths suggest a different mechanism than one large, low-velocity feature that rises into the upper mantle and flows continuously from the southwest to the northeast through the upper mantle (e.g., Bagley & Nyblade, 2013; Forte et al., 2010; Hansen & Nyblade, 2013; Hansen et al., 2012). But this does not preclude lateral mantle flow everywhere beneath the EARS, as our results at shallow upper mantle depths in the east (~100 km, uppermost mantle) appear to suggest continuous low shear velocities (Figure 5c).

5.2.2. Shift of Low Velocities to Western Branch Near MTZ Depths

The African cratons have been modeled as barriers to mantle upwellings, diverting material from the southwest toward the EARS at shallow depth (Forte et al., 2010; Moucha & Forte, 2011). There is also less volcanism along the Western Branch, which may affect rifting processes (Bialas et al., 2010; O'Donnell et al., 2016). In our results, low velocities are imaged in the shallow upper mantle at small, distinct locations along the Western Branch and the southern-southwestern incipient rift arms but are widespread at shallow depths beneath the Main Ethiopian Rift and Afar. The Western Branch, Northern Malawi, and Eastern Branch anomalies are not as slow as the anomalies beneath Afar and the Main Ethiopian Rift (a difference of ~0.1–0.3 km/s); our absolute velocities for the western and eastern branches are in good agreement with velocities from Adams et al. (2012) and O'Donnell et al. (2013) but are faster than predicted by Weeraratne et al. (2003). The shallow upper mantle difference beneath the northeastern and southwestern side of the EARS is likely due to thick lithospheric blocks along the western and southern EARS.

At middle to deep upper mantle depths in the western and southwestern EARS, our model has lower average shear velocities than the northeastern side of the EARS (Figures 4, 5, and supporting information Figure S22). If low-velocity (presumably hot) material is actively upwelling beneath the western sections of the EARS, then part of the material may be diverted eastward by the thick, rigid lithospheric blocks from Turkana/Uganda to Congo and Bangweulu and further south. The asymmetric shape of the Tanzania Craton may also play a role in directing buoyant material eastward.

An alternate explanation to cratonic diversion is that the spatial relationship signifies a temporal history of rising mantle plumes. If a low-velocity plume rose directly upward from the MTZ early during the tectonic history of the EARS, exhausting the low-velocity material near the MTZ, then perhaps the current day low velocity beneath the Western Branch is an indication of what might happen 10+ million years in the future when a deep secondary plume might rise through the upper mantle (e.g., Davaille & Vatteville, 2005; Manga et al., 1993). This interpretation fits with the geodynamic modeling from Koptov et al. (2015) that suggests that asymmetrical melt distributions best fit a plume rising beneath the Eastern Branch.

5.2.3. Velocity-Temperature Relationships

We see remarkably low shear wave velocities beneath the Afar Depression and Main Ethiopian Rift, similar to earlier studies (Table 2; Bastow et al., 2008; Gallacher et al., 2016). We also see very low velocities beneath the Red Sea Rift and western Arabian Peninsula, the Gulf of Aden, the Hoggar and Tibesti Plateaus, and the Cameroon Volcanic Line. Earlier work investigated how low shear velocities can be used to indicate temperature, composition and/or melt; although seismic velocities are strongly influenced by temperature, it is debated whether very low velocities, such as observed beneath Afar, can be solely due to temperature (e.g., Gallacher et al., 2016; Rooney et al., 2012). To explore this, we extract high and low shear velocity values in the upper mantle at hot spot regions and calculate temperature based on two separate approaches from prior studies (see supporting information).

We calculate temperature change based on the 0.7–4.5% per 100 °C from Goes et al. (2000) and also calculate temperature change as a function of seismic velocity perturbation (e.g.,Karato, 1993 ; Rooney et al., 2012), assuming values for activation enthalpy of olivine (Karato, 1993; Rooney et al., 2012) while varying seismic attenuation (Mooney et al., 2003; Venkataraman et al., 2004). For both approaches, predicted temperatures vary widely, depending on the relationship and the parameters assumed. For instance, beneath Afar our velocity is as low as 3.7–3.8 km/s; the temperature predicted by the 4.5% *Vs* relationship of Goes et al. (2000) gives a 100–400 °C range of excess upper mantle temperature, if temperature is the sole cause of the low wave speed, while the 0.7% *Vs* relationship predicts a 1000–2500 °C range of excess temperature. The Karato (1993) relationship gives a 500–1000 °C excess temperature and is highly dependent upon the assumed seismic quality factor (inverse of attenuation), which is not well known beneath Africa (Mooney et al., 2003; Venkataraman et al., 2004). Despite this, nearly all estimates from our minimum shear velocities (with the

exception of the 4.5% *Vs* Goes et al., 2000, relationship) still predicted higher mantle temperatures for the EARS than is suggested by geochemical evidence (Rooney et al., 2012). As proposed by Rooney et al. (2012), the low shear velocities at depths > 200 km in the mantle beneath Africa and the EARS are most likely not produced solely by temperature, but are also dependent on other factors, for example CO2-rich melts (Dasgupta & Hirschmann, 2006). At shallower upper mantle depths, the drastically reduced seismic velocities are likely aided by rift-related decompression melting within a hotter than average upper mantle (e.g., Armitage et al., 2015; Gallacher et al., 2016; Hansen & Nyblade, 2013). Regardless, beneath the northern EARS, our results showing extremely low shear velocities support the interpretation of a thermal or thermochemical anomaly that produces substantial amounts of magma to assist rifting (Bastow et al., 2010; Buck, 2004; Ebinger, 2005; Lavayssière et al., 2018).

5.2.4. Cameroon Volcanic Line

Our results show segmented low-velocity anomalies in the shallow upper mantle (100–200 km) beneath the Cameroon Volcanic Line (CVL); these appear to be the most prominent beneath the northern, central, and southern CVL near recent (<10 Myr) Cenozoic volcanism, and they correspond to previously proposed divisions with the CVL (Burke, 2001; Halliday et al., 1988; Reusch et al., 2010 and references therein). The lowest velocities (4.0–4.3 km/s) in our results are centered toward the north, and as with the EARS, the temperatures predicted from the *Vs* anomalies appear too high in some places to be solely temperature related (Table 2 and supporting information).

The more northern anomaly stretches north toward the Biu and Jos Plateaus (Figures 1 and 8); this pattern agrees well with recent regional surface wave tomography (Adams et al., 2015). But unlike prior studies, which do not resolve structure north of the CVL, our results show a low-velocity anomaly near the base of the upper mantle beneath the western Chad Basin that may be connected to the anomaly at shallow depth beneath the northern CVL (Figure 8). We note that this region may be slightly affected by vertical smearing, so the connection between the deep and shallow anomalies is somewhat uncertain (supporting information Figure S15). However, this pattern has important implications to understanding the formation of the CVL, which is debated due to lack of volcanic age progression along the line (e.g., Njome & de Wit, 2014). In contrast to prior work that attempts to fit one mechanism to this complex pattern of volcanism (Adams et al., 2015; Ojo et al., 2018; Reusch et al., 2010), our results suggest that the northern CVL could be influenced by deeper material from north of the CVL, while a different mechanism may be affecting the south. Our results show distinct low velocities near the top of the upper mantle (<150 km) in the southwestern CVL, but there is no continuation of low velocities at deeper upper mantle depths there; rather shear velocity is close to average or slightly higher than average (Figures 4 and 8). Unless low-velocity material is being sourced from elsewhere in the Atlantic Ocean, where our model loses resolution, this suggests that an edge-driven convection or lithospheric delamination model may be a better fit for the volcanism on the southwestern side of the CVL (e.g., Adams et al., 2015; De Plaen et al., 2014; King & Anderson, 1998; Milelli et al., 2012). However, an influx of deeply sourced material into the northern CVL helps to reconcile some of the debate regarding the overall extent as well as the volcanic processes occurring along the CVL (e.g., Burke, 2001; Gallacher & Bastow, 2012; Njome & de Wit, 2014; Tokam et al., 2010).

5.3. Upper Mantle Structure and Uplifted Topography

Low-velocity features were detected in the shallow upper mantle beneath prominent volcanic plateaus throughout North Africa, including the Hoggar and Tibesti plateaus and the Darfur Dome. While some amount of lateral and/or vertical smearing is expected, particularly in the middle of the Sahara (supporting information Figures S8, S9, and S15), these regions of shallow upper mantle low velocities throughout North Africa may be connected to each other and/or connected to a deep upper mantle or MTZ source. Similar to the plume melt channelization concept explored by Ebinger and Sleep (1998), we note that several of the volcanic domes in this region lie close to or along old rift zones and shear zones (e.g., Njome & de Wit, 2014; Shellnutt et al., 2016), which may connect the anomalies at upper mantle depths. The low upper mantle anomalies throughout North Africa and the CVL are coincident with regions of surface uplift, which agrees with prior studies that suggest uplift due to mantle dynamics (supporting information Figure S25; Burke & Gunnell, 2008; Forte et al., 2010; Müller et al., 2008; Roberts & White, 2010).

Similar to North Africa, the Angola (Bie) Dome in southwestern Africa also shows geological indications of recent uplift (e.g., Burke & Gunnell, 2008; Roberts & White, 2010; Walford & White, 2005; Walker et al.,

2016). Beneath this region, our results show low velocities beneath northwestern Angola from ~100 to 250 km, with the lowest velocities centered just off the coast, between Benguela and Luanda (Figure 6). Dynamic topography has also been invoked for this region to explain the rapid uplift recorded in Cenozoic erosion and sedimentation, and our results further support this idea (e.g., Al-Hajiri et al., 2009; Burke & Gunnell, 2008).

6. Summary and Conclusions

The upper mantle of the African continent has been imaged here using full-wave tomography constrained by fundamental mode Rayleigh waves extracted from long-period ambient noise. The resulting patterns of high and low (isotropic) shear wave speeds match well with the exposed Archean cratons, uplifted plateaus, and Cenozoic volcanism. Our results suggest that the Congo Craton is composed of several smaller cratonic fragments. We also imaged three previously hypothesized cratonic fragments of the North African metacraton and an asymmetric Tanzania cratonic lithosphere that is thinner than the other cratons. Our results suggest that several of these cratonic fragments have notably high velocities, which may be due to compositional differences.

In addition to cratonic structure, we imaged discontinuous patterns of low upper mantle velocities along the length of the EARS. In some cases, these low velocities are much lower than expected for a solely thermal anomaly and are perhaps indicative of melt. These patterns favor a combination of secondary upwellings from or below the MTZ that are diverted and channeled at shallow depths. We find low-velocity anomalies within the shallow upper mantle beneath North Africa, Cameroon, and the Angolan Plateau. These patterns match well with regions of uplifted topography and Cenozoic volcanism. Several of these low-velocity anomalies appear to be connected at shallow depth to the Cameroon Volcanic Line, which may ultimately be partly sourced by a deep upper mantle or MTZ low-velocity anomaly to the north.

Acknowledgments
This work was supported primarily through the National Sciences Foundation Earth Sciences Postdoctoral Fellowship (NSF-EAR 1349684). Additional funds for initial collaboration travel as well as ramp-up and wrap-up time were supplied through NSF (grants OISE-0530062, EAR-0440032, EAR-0824781, and EAR-1634108 through Penn State University and EAR-1516680 and OPP-1643798 through New Mexico Institute of Science and Technology). Additional funds to present this research were supplied by the Computational Infrastructure for Geodynamics (CIG) and the GeoPRISMs Rift Initiation and Evolution TEI. The authors gratefully acknowledge technical support provided by K. Bryan and the computational facilities at the University of Rhode Island. We would like to thank two anonymous reviewers, M. Haney, and Editor M. Long, whose constructive comments helped to improve this paper. We would also like to thank B. Savage, N. Accardo, H. Rotman, J. van Wijk, N. Iverson, and many others for their helpful and insightful discussions regarding this work. All data were requested and obtained from the Incorporated Research Institutions for Seismology Data Management Center (https://www.iris.edu/hq/). The final tomographic model is available online from the IRIS Earth Model Collaboration (http://ds.iris.edu/ds/products/emc-africaantemry-etal2018/). The authors would like to acknowledge that data used in this project originated from several seismic deployments installed and maintained by international groups of Earth scientists, engineers, and technical and logistical support staff. In particular, we would like to thank the community of African geoscientists, who contribute significant efforts to make such deployments possible.

References

Abdelsalam, M. G., Gao, S. S., & Liégeois, J.-P. (2011). Upper mantle structure of the Saharan Metacraton. *Journal of African Earth Sciences*, *60*(5), 328–336. https://doi.org/10.1016/j.jafrearsci.2011.03.009

Abdelsalam, M. G., Liégeois, J.-P., & Stern, R. J. (2002). The Saharan Metacraton. *Journal of African Earth Sciences*, *34*(3-4), 119–136. https://doi.org/10.1016/S0899-5362(02)00013-1

Accardo, N. J., Gaherty, J. B., Shillington, D. J., Ebinger, C. J., Nyblade, A. A., Mbogoni, G. J., Chindandali, P. R. N., et al. (2017). Surface wave imaging of the weakly extended Malawi Rift from ambient-noise and teleseismic Rayleigh waves from onshore and lake-bottom seismometers. *Geophysical Journal International*, *209*(3), 1892–1905. https://doi.org/10.1093/gji/ggx133

Achauer, U., & Masson, F. (2002). Seismic tomography of continental rifts revisited: From relative to absolute heterogeneities. *Tectonophysics*, *358*(1-4), 17–37. https://doi.org/10.1016/S0040-1951(02)00415-8

Adams, A., Miller, J., & Accardo, N. (2018). Relationships between lithospheric structures and rifting in the East African Rift System: A Rayleigh wave tomography study. *Geochemistry, Geophysics, Geosystems*, *19*, 3605–4095. https://doi.org/10.1029/2018GC007750

Adams, A., Nyblade, A., & Weeraratne, D. (2012). Upper mantle shear wave velocity structure beneath the East African plateau: Evidence for a deep, plateauwide low velocity anomaly. *Geophysical Journal International*, *189*(1), 123–142. https://doi.org/10.1111/j.1365-246X.2012.05373.x

Adams, A. N., Wiens, D. A., Nyblade, A. A., Euler, G. G., Shore, P. J., & Tibi, R. (2015). Lithospheric instability and the source of the Cameroon Volcanic Line: Evidence from Rayleigh wave phase velocity tomography. *Journal of Geophysical Research: Solid Earth*, *120*, 1708–1727. https://doi.org/10.1002/2014JB011580

Albuquerque Seismological Laboratory (ASL)/USGS (1988). Global seismograph network (GSN-IRIS/USGS). International federation of digital seismograph networks, Other/Seismic Network. https://doi.org/10.7914/SN/IU

Albuquerque Seismological Laboratory (ASL)/USGS (1993). Global telemetered seismograph network (USAF/USGS). International Federation of Digital Seismograph Networks, Other/Seismic Network. https://doi.org/10.7914/SN/GT

Al-Hajiri, Y., White, N., & Fishwick, S. (2009). Scales of transient convective support beneath Africa. *Geology*, *37*(10), 883–886. https://doi.org/10.1130/G25703A.1

Amante, C. and B.W. Eakins (2009). ETOPO1 1 arc-minute global relief model: Procedures, data sources and analysis, *NOAA Technical Memorandum NESDIS NGDC*-24, National Geophysical Data Center, NOAA. https://doi.org/10.7289/V5C8276M

Andreoli, M. A. G. (1984). Petrochemistry, tectonic evolution and metasomatic mineralisations of Mozambique Belt granulites from S. Malawi and Tete (Mozambique). *Precambrian Research*, *25*(1-3), 161–186. https://doi.org/10.1016/0301-9268(84)90031-7

Andriampenomanana, F., Nyblade, A. A., Wysession, M. E., Durrheim, R. J., Tilmann, F., Julià, J., Pratt, M. J., et al. (2017). The structure of the crust and uppermost mantle of Madagascar. *Geophysical Journal International*, *210*(3), 1525–1544. https://doi.org/10.1093/gji/ggx243

Armitage, J. J., Ferguson, D. J., Goes, S., Hammond, J. O. S., Calais, E., Rychert, C. A., & Harmon, N. (2015). Upper mantle temperature and the onset of extension and break-up in Afar, Africa. *Earth and Planetary Science Letters*, *418*, 78–90. https://doi.org/10.1016/j.epsl.2015.02.039

Ayadi, A., Dorbath, C., Lesquer, A., & Bezzeghoud, M. (2000). Crustal and upper mantle velocity structure of the Hoggar swell (Central Sahara, Algeria). *Physics of the Earth and Planetary Interiors*, *118*(1-2), 111–123. https://doi.org/10.1016/S0031-9201(99)00134-X

Bagley, B., & Nyblade, A. A. (2013). Seismic anisotropy in eastern Africa, mantle flow, and the African superplume. *Geophysical Research Letters*, *40*, 1500–1505. https://doi.org/10.1002/grl.50315

Bastow, I. D. (2012). Relative arrival-time upper-mantle tomography and the elusive background mean. *Geophysical Journal International*, *190*(2), 1271–1278. https://doi.org/10.1111/j.1365-246X.2012.05559.x

Bastow, I. D., Nyblade, A. A., Stuart, G. W., Rooney, T. O., & Benoit, M. H. (2008). Upper mantle seismic structure beneath the Ethiopian hot spot: Rifting at the edge of the African low-velocity anomaly. *Geochemistry, Geophysics, Geosystems*, *9*, Q12022. https://doi.org/10.1029/2008GC002107

Bastow, I. D., Pilidou, S., Kendall, J.-M., & Stuart, G. W. (2010). Melt-induced seismic anisotropy and magma assisted rifting in Ethiopia: Evidence from surface waves. *Geochemistry, Geophysics, Geosystems*, *11*, Q0AB05. https://doi.org/10.1029/2010GC003036

Bastow, I. D., Stuart, G. W., Kendall, J.-M., & Ebinger, C. J. (2005). Upper-mantle seismic structure in a region of incipient continental breakup: Northern Ethiopian rift. *Geophysical Journal International*, *162*(2), 479–493. https://doi.org/10.1111/j.1365-246X.2005.02666.x

Batumike, J. M., Griffin, W. L., & O'Reilly, S. Y. (2009). Lithospheric mantle structure and the diamond potential of kimberlites in southern D.R. Congo. *Lithos*, *112S*, 166–176. https://doi.org/10.1016/j.lithos.2009.04.020

Beck, S. & Zandt, G. (2005). Continental lithospheric deformation along a major strike-slip fault zone: the central North Anatolian Fault Zone, Turkey. International Federation of Digital Seismograph Networks, Other/Seismic Network. https://doi.org/10.7914/SN/YL_2005

Begg, G. C., Griffin, W. L., Natapov, L. M., O'Reilly, S. Y., Grand, S. P., O'Neill, C. J., Hronsky, J. M. A., et al. (2009). The lithospheric architecture of Africa: Seismic tomography, mantle petrology, and tectonic evolution. *Geosphere*, *5*(1), 23–50. https://doi.org/10.1130/GES00179.1

Benoit, M. H., Nyblade, A. A., Owens, T. J., & Stuart, G. (2006)). Mantle transition zone structure and upper mantle S velocity variations beneath Ethiopia: Evidence for a broad, deep-seated thermal anomaly. *Geochemistry, Geophysics, Geosystems*, *7*, Q11013. https://doi.org/10.1029/2006GC001398

Benoit, M. H., Nyblade, A. A., & Pasyanos, M. E. (2006). Crustal thinning between the Ethiopian and East African plateaus from modeling Rayleigh wave dispersion. *Geophysical Research Letters*, *33*, L13301. https://doi.org/10.1029/2006GL025687

Benoit, M. H., Nyblade, A. A., & VanDecar, J. C. (2006). Upper mantle P-wave speed variations beneath Ethiopia and the origin of the Afar hotspot. *Geology*, *34*(5), 329–332. https://doi.org/10.1130/G22281.1

Benoit, M. H., Nyblade, A. A., VanDecar, J. C., & Gurrola, H. (2003). Upper mantle P wave velocity structure and transition zone thickness beneath the Arabian Shield. *Geophysical Research Letters*, *30*(10), 1531. https://doi.org/10.1029/2002GL016436

Bensen, G. D., Ritzwoller, M. H., Barmin, M. P., Levshin, A. L., Lin, F., Moschetti, M. P., Shapiro, N. M., et al. (2007). Processing seismic ambient noise data to obtain reliable broad-band surface wave dispersion measurements. *Geophysical Journal International*, *169*(3), 1239–1260. https://doi.org/10.1111/j.1365-246X.2007.03374.x

Bialas, R. W., Buck, W. R., & Qin, R. (2010). How much magma is required to rift a continent? *Earth and Planetary Science Letters*, *292*(1-2), 68–78. https://doi.org/10.1016/j.epsl.2010.01.021

Brazier, R. A., Nyblade, A. A., Langston, C. A., & Owens, T. J. (2000). Pn wave velocities beneath the Tanzania Craton and adjacent rifted mobile belts, East Africa. *Geophysical Research Letters*, *27*(16), 2365–2368. https://doi.org/10.1029/2000GL011586

Buck, W. R. (2004). Consequences of asthenospheric variability on continental rifting. In G. Karner, B. Taylor, N. W. Driscoll, & D. L. Kohlstedt (Eds.), *Rheology and deformation of the lithosphere at continental margins*, (pp. 1–30). New York: Columbia University Press. https://doi.org/10.7312/karn12738

Buehler, J. S., & Shearer, P. M. (2016). Characterizing earthquake location uncertainty in North America using source-receiver reciprocity and USArray. *Bulletin of the Seismological Society of America*, *106*(5), 2395–2401. https://doi.org/10.1785/0120150173

Bufford, K. M., Atekwana, E. A., Abdelsalam, M. G., Shemang, E., Atekwana, E. A., Mickus, K., Moidaki, M., et al. (2012). Geometry and faults tectonic activity of the Okavango Rift Zone, Botswana: Evidence from magnetotelluric and electrical resistivity tomography imaging. *Journal of African Earth Sciences*, *65*, 61–71. https://doi.org/10.1016/j.jafrearsci.2012.01.004

Buiter, S. J. H., Steinberger, B., Medvedev, S., & Tetreault, J. L. (2012). Could the mantle have caused subsidence of the Congo Basin? *Tectonophysics*, *514-517*, 62–80. https://doi.org/10.1016/j.tecto.2011.09.024

Burke, K. (2001). Origin of the Cameroon Line of volcano-capped swells. *Journal of Geology*, *109*(3), 349–362. https://doi.org/10.1086/319977

Burke, K., & Gunnell, Y. (2008). The African erosion surface: A continental-scale synthesis of geomorphology, tectonics, and environmental change over the past 180 million years. *GSA Memoir*, *201*, 66. https://doi.org/10.1130/2008.1201

Canil, D. (2004). Mildly incompatible elements in peridotites and the origins of mantle lithosphere. *Lithos*, *77*(1-4), 375–393. https://doi.org/10.1016/j.lithos.2004.04.014

Cao, Q., van der Hilst, R. D., de Hoop, M. V., & Shim, S.-H. (2011). Seismic imaging of transition zone discontinuities suggests hot mantle west of Hawaii. *Science*, *332*(6033), 1068–1071. https://doi.org/10.1126/science.1202731

Chang, S.-J., & van der Lee, S. (2011). Mantle plumes and associated flow beneath Arabia and East Africa. *Earth and Planetary Science Letters*, *302*(3-4), 448–454. https://doi.org/10.1016/j.epsl.2010.12.050

Chardon, D., Grimaud, J.-L., Beauvais, A., & Bamba, O. (2018). West African lateritic pediments: Landform-regolith evolution processes and mineral exploration pitfalls. *Earth-Science Reviews*, *179*, 124–146. https://doi.org/10.1016/j.earscirev.2018.02.009

Chen, P., Jordan, T. H., & Zhao, L. (2007). Full three-dimensional tomography: A comparison between the scattering-integral and adjoint-wavefield methods. *Geophysical Journal International*, *170*(1), 175–181. https://doi.org/10.1111/j.1365-246X.2007.03429.x

Chorowicz, J. (2005). The East African rift system. *Journal of African Earth Sciences*, *43*(1-3), 379–410. https://doi.org/10.1016/j.jafrearsci.2005.07.019

Christensen, N. I., & Mooney, W. D. (1995). Seismic velocity structure and composition of the continental crust: A global view. *Journal of Geophysical Research*, *100*(B7), 9761–9788. https://doi.org/10.1029/95JB00259

Christensen, U. R., & Yuen, D. A. (1985). Layered convection induced by phase transitions. *Journal of Geophysical Research*, *90*(B12), 10,291–10,300. https://doi.org/10.1029/JB090iB12p10291

Civiero, C., Goes, S., Hammond, J. O. S., Fishwick, S., Ahmed, A., Ayele, A., Doubre, C., et al. (2016). Small-scale thermal upwellings under the northern East African Rift from S travel time tomography. *Journal of Geophysical Research: Solid Earth*, *121*, 7395–7408. https://doi.org/10.1002/2016JB013070

Civiero, C., Hammond, J. O. S., Goes, S., Fishwick, S., Ahmed, A., Ayele, A., Doubre, C., et al. (2015). Multiple mantle upwellings in the transition zone beneath the northern East-African Rift system from relative P-wave travel-time tomography. *Geochemistry, Geophysics, Geosystems*, *16*, 2949–2968. https://doi.org/10.1002/2015GC005948

Colli, L., Fichtner, A., & Bunge, H.-P. (2013). Full waveform tomography of the upper mantle in the South Atlantic region: Imaging a westward fluxing shallow asthenosphere? *Tectonophysics*, *604*, 26–40. https://doi.org/10.1016/j.tecto.2013.06.015

Collins, A. S., & Piesarevsky, S. A. (2005). Amalgamating eastern Gondwana: The evolution of the Circum-Indian Orogens. *Earth-Science Reviews*, *71*(3-4), 229–270. https://doi.org/10.1016/j.earscirev.2005.02.004

Corbeau, J., Rolandon, F., Leroy, S., Al-Lazki, A., Stork, A. L., Keir, D., Stuart, G. W., et al. (2014). Uppermost mantle velocity from Pn tomography in the Gulf of Aden. *Geosphere*, *10*(5), 958–968. https://doi.org/10.1130/GES01052.1

Corchete, V. (2013). Shear-wave velocity structure of Africa from Rayleigh-wave analysis. *International Journal of Earth Sciences*, *102*(3), 857–873. https://doi.org/10.1007/s00531-012-0827-7

Cornwell, D. G., Hetényi, G., & Blanchard, T. D. (2011). Mantle transition zone variations beneath the Ethiopian Rift and Afar: Chemical heterogeneity within a hot mantle? *Geophysical Research Letters*, *38*, L16308. https://doi.org/10.1029/2011GL047575

Corti, G. (2009). Continental rift evolution: From rift initiation to incipient break-up in the Main Ethiopian Rift, East Africa. *Earth-Science Reviews*, *96*(1-2), 1–53. https://doi.org/10.1016/j.earscirev.2009.06.005

Covellone, B. M., Savage, B., & Shen, Y. (2015). Seismic wave speed structure of the Ontong Java Plateau. *Earth and Planetary Science Letters*, *420*, 140–150. https://doi.org/10.1016/j.epsl.2015.03.033

Crosby, A. G., Fishwick, S., & White, N. (2010). Structure and evolution of the intracratonic Congo Basin. *Geochemistry, Geophysics, Geosystems*, *11*, Q06010. https://doi.org/10.1029/2009GC003014

Daly, M. C., Lawrence, S. R., Kimun'a, D., & Binga, M. (1991). Late Paleozoic deformation in central Africa: A result of distant collision? *Nature*, *350*, 605–607. https://doi.org/10.1038/350605a0

Darbyshire, F. A., Eaton, D. W., & Bastow, I. D. (2013). Seismic imaging of the lithosphere beneath the Hudson Bay: Episodic growth of the Laurentian mantle keel. *Earth and Planetary Science Letters*, *373*, 179–193. https://doi.org/10.1016/j.epsl.2013.05.002

Dasgupta, R., & Hirschmann, M. M. (2006). Melting in the Earth's deep upper mantle caused by carbon dioxide. *Nature*, *440*, 659–662. https://doi.org/10.1038/nature04612

Davaille, A., & Vatteville, J. (2005). On the transient nature of mantle plumes. *Geophysical Research Letters*, *32*, L14309. https://doi.org/10.1029/2005GL023029

Dave, R., & Li, A. (2016). Destruction of the Wyoming craton: Seismic evidence and geodynamic processes. *Geology*, *44*(11), 883–886. https://doi.org/10.1130/G38147.1

De Plaen, R. S. M., Bastow, I. D., Chambers, E. L., Keir, D., Gallacher, R. J., & Keane, J. (2014). The development of magmatism along the Cameroon Volcanic Line: Evidence from seismicity and seismic anisotropy. *Journal of Geophysical Research: Solid Earth*, *119*, 4233–4252. https://doi.org/10.1002/2013JB010583

de Wit, M. J., Stankiewicz, J., & Reeves, C. (2008). Restoring Pan-African-Brasiliano connections: More Gondwana control, less Trans-Atlantic corruption. *Geological Society, London, Special Publications*, *294*, 399–412. https://doi.org/10.1144/SP294.20

Dorbath, C., Dorbath, L., Fairhead, J. D., & Stuart, G. W. (1986). A teleseismic delay time study across the Central African Shear Zone in the Adamawa region of Cameroon, West Africa. *Geophysical Journal International*, *86*(3), 751–766. https://doi.org/10.1111/j.1365-246X.1986.tb00658.x

Downey, N. J., & Gurnis, M. (2009). Instantaneous dynamics of the cratonic Congo basin. *Journal of Geophysical Research*, *114*, B06401. https://doi.org/10.1029/2008JB006066

Dugda, M., Nyblade, A. A., & Julià, J. (2007). Thin lithosphere beneath the Ethiopian Plateau revealed by a joint inversion of Rayleigh wave group velocities and receiver functions. *Journal of Geophysical Research*, *112*, B08305. https://doi.org/10.1029/2006JB004918

Dugda, M. T., Nyblade, A. A., & Julià, J. (2009). S-wave velocity structure of the crust and upper mantle beneath Kenya in comparison to Tanzania and Ethiopia: Implications for the formation of the East African and Ethiopian Plateaus. *South African Journal of Geology*, *112*(3-4), 241–250. https://doi.org/10.2113/gssajg.112.3-4.241

Eaton, D. W., Darbyshire, F., Evans, R. L., Grütter, H., Jones, A. G., & Yuan, X. (2009). The elusive lithosphere-asthenosphere boundary (LAB) beneath cratons. *Lithos*, *109*(1-2), 1–22. https://doi.org/10.1016/j.lithos.2008.05.009

Ebinger, C. (2005). Continental break-up: The East African perspective. *Astronomy & Geophysics*, *46*(2), 2.16–2.21. https://doi.org/10.1111/j.1468-4004.2005.46216.x

Ebinger, C., Poudjom Djomani, Y., Mbede, E., Foster, A., & Dawson, J. B. (1997). Rifting Archean lithosphere: The Eyasi-Manyara-Natron rifts, East Africa. *Journal of the Geological Society*, *154*, 947–960. https://doi.org/10.1144/gsjgs.154.6.0947

Ebinger, C. J., Keir, D., Bastow, I. D., Whaler, K., Hammond, J. O. S., Ayele, A., Miller, M. S., et al. (2017). Crustal structure of active deformation zones in Africa: Implications for global crustal processes. *Tectonics*, *36*, 3298–3332. https://doi.org/10.1002/2017TC004526

Ebinger, C. J., & Sleep, N. H. (1998). Cenozoic magmatism throughout east Africa resulting from impact of a single plume. *Nature*, *395*, 788–791. https://doi.org/10.1038/27417

Ebinger, C. J., Yemane, T., Harding, D. J., Tesfaye, S., Kelley, S., & Rex, D. C. (2000). Rift deflection, migration, and propagation: Linkage of the Ethiopian and Eastern rifts, Africa. *GSA Bulletin*, *112*(2), 163–176. https://doi.org/10.1130/0016-7606(2000)112<163:RDMAPL>2.0.CO;2

Emry, E. L., Wiens, D. A., Shiobara, H., & Sugioka, H. (2011). Seismogenic characteristics of the Northern Mariana shallow thrust zone from local array data. *Geochemistry, Geophysics, Geosystems*, *12*, Q12008. https://doi.org/10.1029/2011GC003853

Ennih, N., & Liégeois, J.-P. (2008). The boundaries of the West African craton, with special reference to the basement of the Moroccan metacratonic Anti-Atlas belt. *Geological Society, London, Special Publications*, *297*, 1–17. https://doi.org/10.1144/SP297.1

Fezaa, N., Liégeois, J.-P., Abdallah, N., Cherfouh, E.-H., De Waele, B., Bruguier, O., & Ouabadi, A. (2010). Late Ediacaran geological evolution (575-555 Ma) of the Djanet Terrane, Eastern Hoggar, Algeria, evidence for a Murzukian intracontinental episode. *Precambrian Research*, *180*(3-4), 299–327. https://doi.org/10.1016/j.precamres.2010.05.011

Fichtner, A., Kennett, B. L. N., Igel, H., & Bunge, H.-P. (2009). Full seismic waveform tomography for upper-mantle structure in the Australasian region using adjoint methods. *Geophysical Journal International*, *179*(3), 1703–1725. https://doi.org/10.1111/j.1365-246X.2009.04368.x

Fichtner, A., Trampert, J., Cupillard, P., Saygin, E., Taymaz, T., Capdeville, Y., & Villaseñor, A. (2013). Multiscale full waveform inversion. *Geophysical Journal International*, *194*(1), 534–556. https://doi.org/10.1093/gji/ggt118

Fichtner, A., & Villaseñor, A. (2015). Crust and upper mantle of the western Mediterranean—Constraints from full-waveform inversion. *Earth and Planetary Science Letters*, *428*, 52–62. https://doi.org/10.1016/j.epsl.2015.07.038

Fischer, K. M., Ford, H. A., Abt, D. L., & Rychert, C. A. (2010). The lithosphere-asthenosphere boundary. *Annual Review of Earth and Planetary Sciences*, *38*, 551–575. https://doi.org/10.1146/annurev-earth-040809-152438

Fishwick, S. (2010). Surface wave tomography: Imaging of the lithosphere-asthenosphere boundary beneath central and southern Africa? *Lithos*, *120*(1-2), 63–73. https://doi.org/10.1016/j.lithos.2010.05.011

Fishwick, S., & Bastow, I. D. (2011). Towards a better understanding of African topography: A review of passive-source seismic studies of the African crust and upper mantle. *Geological Society, London, Special Publications*, *357*, 343–371. https://doi.org/10.1144/SP357.19

Forte, A. M., Quéré, S., Moucha, R., Simmons, N. A., Grand, S. P., Mitrovica, J. X., & Rowley, D. B. (2010). Joint seismic-geodynamic-mineral physical modelling of African geodynamics: A reconciliation of deep-mantle convection with surface geophysical constraints. *Earth and Planetary Science Letters*, *295*(3-4), 329–341. https://doi.org/10.1016/j.epsl.2010.03.017

French, S. W., & Romanowicz, B. (2015). Broad plumes rooted at the base of the Earth's mantle beneath major hotspots. *Nature*, *525*, 95–99. https://doi.org/10.1038/nature14876

Furman, T. (2007). Geochemistry of East African Rift basalts: An overview. *Journal of African Earth Sciences*, *48*(2-3), 147–160. https://doi.org/10.1016/j.jafrearsci.2006.06.009

Furman, T., Bryce, J., Rooney, T., Hanan, B., Yirgu, G., & Ayalew, D. (2006). Heads and tails: 30 million years of the Afar plume. In G. Yirgu, C. J. Ebinger, & P. K. H. Maguire (Eds.), *The structure and evolution of the East African rift system in the afar volcanic province*, *Geological Society of London Special Publications*, (Vol. 259, pp. 95–119). https://doi.org/10.1144/GSL.SP.2006.259.01.09

Gallacher, R. J., & Bastow, I. D. (2012). The development of magmatism along the Cameroon Volcanic Line: Evidence from teleseismic receiver function. *Tectonics*, *31*, TC3018. https://doi.org/10.1029/2011TC003028

Gallacher, R. J., Keir, D., Harmon, N., Stuart, G., Leroy, S., Hammond, J. O. S., Kendall, J.-M., et al. (2016). The initiation of segmented buoyancy-driven melting during continental breakup. *Nature Communications*, *7*, 13110. https://doi.org/10.1038/ncomms13110

Gao, H., & Shen, Y. (2012). Validation of shear-wave velocity models of the Pacific Northwest. *Bulletin of the Seismological Society of America*, *102*(6), 2611–2621. https://doi.org/10.1785/0120110336

Gao, H., & Shen, Y. (2014). Upper mantle structure of the Cascades from full-wave ambient noise tomography: Evidence for 3D mantle upwelling in the back-arc. *Earth and Planetary Science Letters*, *390*, 222–233. https://doi.org/10.1016/j.epsl.2014.01.012

Gao, H., & Shen, Y. (2015). Validation of recent shear wave velocity models in the United States with full-wave simulation. *Journal of Geophysical Research: Solid Earth*, *120*, 534–358. https://doi.org/10.1002/2014JB011369

Gao, S. (2009). Four-dimensional anatomy of continental rifts transitioning into sea floor spreading: Insights from Afar, Ethiopia for oil and gas exploration of global rift systems and passive continental margins. International Federation of Digital Seismograph Networks, Other/Seismic Network. https://doi.org/10.7914/SN/ZK_2009

Gao, S., Rudnick, R. L., Xu, W.-L., Yuan, H.-L., Liu, Y.-S., Walker, R. J., Puchtel, I. S., et al. (2008). Recycling deep cratonic lithosphere and generation of intraplate magmatism in the North China Craton. *Earth and Planetary Science Letters*, *270*, 41–53. https://doi.org/10.1016/j.epsl.2008.03.008

Garber, J. M., Maurya, S., Hernandez, J.-A., Duncan, M. S., Zeng, L., Zhang, H. L., Faul, U., et al. (2018). Multidisciplinary constraints on the abundance of diamond and eclogite in the cratonic lithosphere. *Geochemistry, Geophysics, Geosystems*, *19*, 2062–2086. https://doi.org/10.1029/2018GC007534

GEOFON data centre (1993). GEOFON seismic network, Deutsches GeoForschungsZentrum GFZ. https://doi.org/10.14470/tr560404

Goes, S., Govers, R., & Vacher, P. (2000). Shallow mantle temperatures under Europe from P and S wave tomography. *Journal of Geophysical Research*, *105*(B5), 11,153–11,169. https://doi.org/10.1029/1999JB900300

Göğüş, O. H., Pysklywec, R. N., Şengör, A. M. C., & Gün, E. (2017). Drip tectonics and the enigmatic uplift of the Central Anatolian Plateau. *Nature Communications*, *8*, 1538. https://doi.org/10.1038/s41467-017-01611-3

Grand, S. P. (2000). Mantle shear-wave tomography and the fate of subducted slabs. *Philosophical Transactions of the Royal Society A*, *360*, 2475–2491. https://doi.org/10.1098/rsta.2002.1077

Green, W. V., Achauer, U., & Meyer, R. P. (1991). A three-dimensional seismic image of the crust and upper mantle beneath the Kenya rift. *Nature*, *354*, 199–203. https://doi.org/10.1038/354199a0

Griffin, W. L., O'Reilly, S. Y., Afonso, J. C., & Begg, G. C. (2009). The composition and evolution of lithospheric mantle: A re-evaluation and its tectonic implications. *Journal of Petrology*, *50*(7), 1185–1204. https://doi.org/10.1093/petrology/egn033

Grijalva, A., Nyblade, A. A., Homman, K., Accardo, N. J., Gaherty, J. B., Ebinger, C. J., Shillington, D. J., et al. (2018). Seismic evidence for plume- and craton-influenced upper mantle structure beneath the northern Malawi rift and the Rungwe volcanic province, East Africa. *Geochemistry, Geophysics, Geosystems*, *19*, 3980–3994. https://doi.org/10.1029/2018GC007730

Guirard, R., Mbaigane, J.-C. D., Carretier, S., & Dominguez, S. (2000). Evidence for a 6000 km length NW-SE-striking lineament in northern Africa: The Tibesti Lineament. *Journal of the Geological Society*, *157*(5), 897–900. https://doi.org/10.1144/jgs.157.5.897

Hager, B. H., Clayton, R. W., Richards, M. A., Comer, R. P., & Dziewonski, A. M. (1985). Lower mantle heterogeneity, dynamic topography and the geoid. *Nature*, *313*, 541–545. https://doi.org/10.1038/313541a0

Halliday, A. N., Dickin, A. P., Fallick, A. E., & Fitton, J. G. (1988). Mantle dynamics: A Nd, Sr, Pb and O isotopic study of the Cameroon Line Volcanic Chain. *Journal of Petrology*, *29*(1), 181–211. https://doi.org/10.1093/petrology/29.1.181

Hammond, J. O. S., Kendall, J.-M., Stuart, G. W., Ebinger, C. J., Bastow, I. D., Keir, D., Ayele, A., et al. (2013). Mantle upwelling and intiation of rift segmentation beneath the Afar Depression. *Geology*, *41*(6), 635–638. https://doi.org/10.1130/G33925.1

Hansen, S., Schwartz, S., Al-Amri, A., & Rodgers, A. (2006). Combined plate motion and density-driven flow in the asthenosphere beneath Saudi Arabia: Evidence from shear-wave splitting and seismic anisotropy. *Geology*, *34*(10), 869–872. https://doi.org/10.1130/G22713.1

Hansen, S. E., & Nyblade, A. A. (2013). The deep seismic structure of the Ethiopia/Afar hotspot and the African superplume. *Geophysical Journal International*, *194*(1), 118–124. https://doi.org/10.1093/gji/ggt116

Hansen, S. E., Nyblade, A. A., & Benoit, M. H. (2012). Mantle structure beneath Africa and Arabia from adaptively parameterized P-wave tomography: Implications for the origin of Cenozoic Afro-Arabian tectonism. *Earth and Planetary Science Letters*, *319-320*, 23–34. https://doi.org/10.1016/j.epsl.2011.12.023

Hartley, R. W., & Allen, P. A. (1994). Interior cratonic basins of Africa: Relation to continental break-up and role of mantle convection. *Basin Research*, *6*, 95–113. https://doi.org/10.1111/j.1365-2117.1994.tb00078.x

Hirth, G., Evans, R. L., & Chave, A. D. (2000). Comparison of continental and oceanic mantle electrical conductivity: Is the Archean lithosphere dry? *Geochemistry, Geophysics, Geosystems*, *1*. https://doi.org/10.1029/2000GC000048

Hopper, E., & Fischer, K. M. (2015). The meaning of the midlithospheric discontinuities: A case study in the northern U.S. craton. *Geochemistry, Geophysics, Geosystems*, *16*, 4057–4083. https://doi.org/10.1002/2015GC006030

Houser, C., Masters, G., Shearer, P., & Laske, G. (2008). Shear and compressional velocity models of the mantle from cluster analysis of long-period waveforms. *Geophysical Journal International*, *174*(1), 195–212. https://doi.org/10.1111/j.1365-246X.2008.03763.x

Huerta, A. D., Nyblade, A. A., & Reusch, A. M. (2009). Mantle transition zone structure beneath Kenya and Tanzania: More evidence for a deep-seated thermal upwelling in the mantle. *Geophysical Journal International*, *177*(3), 1249–1255. https://doi.org/10.1111/j.1365-246X.2009.04092.x

Institut De Physique Du Globe De Paris (IPGP), & Ecole Et Observatoire Des Sciences De La Terre De Strasbourg (EOST) (1982). GEOSCOPE, French Global Network of broad band seismic stations, Institut de Physique du Globe de Paris (IPGP). https://doi.org/10.18715/geoscope.g

Jakovlev, A., Rümpker, G., Schmeling, H., Koulakov, I., Lindenfeld, M., & Wallner, H. (2013). Seismic images of magmatic rifting beneath the western branch of the East African rift. *Geochemistry, Geophysics, Geosystems*, *14*, 4906–4920. https://doi.org/10.1002/2013GC004939

Jessell, M. W., Begg, G. C., & Miller, M. S. (2016). The geophysical signatures of the West African Craton. *Precambrian Research*, *274*, 3–24. https://doi.org/10.1016/j.precamres.2015.08.010

Kadima, E., Delvaux, D., Sebagenzi, S. N., Tack, L., & Kabeya, S. M. (2011). Structure and geological history of the Congo Basin: An integrated interpretation of gravity, magnetic and reflection seismic data. *Basin Research*, *23*, 499–527. https://doi.org/10.1111/j.1365-2117.2011.00500.x

Karato, S. (1993). Importance of anelasticity in the interpretation of seismic tomography. *Geophysical Research Letters*, *20*(15), 1623–1626. https://doi.org/10.1029/93GL01767

Karato, S., Olugboji, T., & Park, J. (2015). Mechanisms and geologic significance of the mid-lithosphere discontinuity in the continents. *Nature Geoscience*, *8*, 509–514. https://doi.org/10.1038/NGEO2462

Katumwehe, A. B., Abdelsalam, M. G., & Atekwana, E. A. (2015). The role of pre-existing Precambrian structures in rift evolution: The Albertine and Rhino grabens, Uganda. *Tectonophysics*, *646*, 117–129. https://doi.org/10.1016/j.tecto.2015.01.022

Kennett, B. L. N., Engdahl, E. R., & Buland, R. (1995). Constraints on seismic velocities in the Earth from travel times. *Geophysical Journal International*, *122*(1), 108–124. https://doi.org/10.1111/j.1365-246X.1995.tb03540.x

Keranen, K. M., Klemperer, S. L., Julià, J., Lawrence, J. F., & Nyblade, A. A. (2009). Low lower crustal velocity across Ethiopia: Is the Main Ethiopian Rift a narrow rift in a hot craton? *Geochemistry, Geophysics, Geosystems*, *10*, Q0AB01. https://doi.org/10.1029/2008GC002293

Khoza, T. D., Jones, A. G., Muller, M. R., Evans, R. L., Miensopust, M. P., & Webb, S. J. (2013). Lithospheric structure of an Archean craton and adjacent mobile belt revealed from 2-D and 3-D inversion of magnetotelluric data: Example from southern Congo craton in northern Namibia. *Journal of Geophysical Research: Solid Earth*, *118*, 4378–4397. https://doi.org/10.1002/jgrb.50258

Kieffer, B., Arndt, N., Lapierre, H., Bastien, F., Bosch, D., Pecher, A., Yirgu, G., et al. (2004). Flood and shield basalts from Ethiopia: Magmas from the African superswell. *Journal of Petrology*, *45*(4), 793–834. https://doi.org/10.1093/petrology/egg112

King, S. D., & Anderson, D. L. (1998). Edge-driven convection. *Earth and Planetary Science Letters*, *160*(3-4), 289–296. https://doi.org/10.1016/S0012-821X(98)00089-2

Koornneef, J. M., Davies, G. R., Dopp, S. P., Vukmanovic, Z., Nikogosian, I. K., & Mason, P. R. D. (2009). Nature and timing of multiple metasomatic events in the sub-cratonic lithosphere beneath Labait, Tanzania. *Lithos*, *112S*, 896–912. https://doi.org/10.1016/j.lithos.2009.04.039

Koptov, A., Calais, E., Burov, E., Leroy, S., & Gerya, T. (2015). Dual continental rift systems generated by plume-lithosphere interaction. *Nature Geoscience*, *8*, 388–392. https://doi.org/10.1038/ngeo2401

Korostelev, F., Leroy, S., Keir, D., Ahmed, A., Boschi, L., Rolandone, F., Stuart, G. W., et al. (2015). Upper mantle structure of the southern Arabian margin: Insights from teleseismic tomography. *Geosphere*, *11*(5), 1262–1278. https://doi.org/10.1130/GES01159.1

Korostelev, F., Leroy, S., Keir, D., Weemstra, C., Boschi, L., Molinari, I., Ahmed, A., et al. (2016). Magmatism at continental passive margins inferred from ambient-noise phase-velocity in the Gulf of Aden. *Terra Nova*, *28*, 19–26. https://doi.org/10.1111/ter.12182

Laske, G., Masters, G., Ma, Z., & Pasyanos, M. (2013). Update on CRUST1.0—A 1-degree global model of Earth's crust. Geophysical Research Abstracts, 15, Abstract EGU2013-2658.

Lavayssière, A., Rychert, C., Harmon, N., Keir, D., Hammond, J. O. S., Kendall, J.-M., Doubre, C., et al. (2018). Imaging lithospheric discontinuities beneath the Northern East African Rift using S-to-P receiver functions. *Geochemistry, Geophysics, Geosystems*, *19*, 4048–4062. https://doi.org/10.1029/2018GC007463

Lee, C.-T. A., Luffi, P., & Chin, E. J. (2011). Building and destroying the continental mantle. *Annual Review of Earth and Planetary Sciences*, *39*, 59–90. https://doi.org/10.1146/annurev-earth-040610-133505

Leseane, K., Atekwana, E. A., Mickus, K. L., Abdelsalam, M. G., Shemang, E. M., & Atekwana, E. A. (2015). Thermal perturbations beneath the incipient Okavango Rift Zone, northwest Botswana. *Journal of Geophysical Research: Solid Earth*, *120*, 1210–1228. https://doi.org/10.1002/2014JB011029

Liégeois, J.-P., Abdelsalam, M. G., Ennih, N., & Ouabadi, A. (2013). Matacraton: Nature, genesis, and behavior. *Gondwana Research*, *23*(1), 220–237. https://doi.org/10.1016/j.gr.2012.02.016

Lithgow-Bertelloni, C., & Silver, P. G. (1998). Dynamic topography, plate driving forces, and the African superswell. *Nature*, *395*, 269–272. https://doi.org/10.1038/26212

Maceira, M., Larmat, C., Porritt, R. W., Higdon, D. M., Rowe, C. A., & Allen, R. M. (2015). On the validation of seismic imaging methods: Finite frequency or ray theory? *Geophysical Research Letters*, *42*, 323–330. https://doi.org/10.1002/2014GL062571

Manga, M., Stone, H. A., & O'Connell, R. J. (1993). The interaction of plume heads with compositional discontinuities in the Earth's mantle. *Journal of Geophysical Research*, *98*(B11), 19,979–19,990. https://doi.org/10.1029/93JB00441

McGregor, D. (2015). History of the development of the East African Rift System: A series of interpreted maps through time. *Journal of African Earth Sciences*, *101*, 232–252. https://doi.org/10.1016/j.jafrearsci.2014.09.016

MedNet Project Partner Institutions (1990). *Mediterranean very broadband seismographic network (MedNet)*. Italy: Istituto Nazionale di Geofisica e Vulcanologia (INGV). https://doi.org/10.13127/sd/fbbbtdtd6q

Milelli, L., Fourel, L., & Jaupart, C. (2012). A lithospheric instability origin for the Cameroon Volcanic Line. *Earth and Planetary Science Letters*, *335-336*, 80–87. https://doi.org/10.1016/j.epsl.2012.04.028

Montelli, R., Nolet, G., Dahlen, F. A., & Masters, G. (2006). A catalogue of deep mantle plumes: New results from finite-frequency tomography. *Geochemistry, Geophysics, Geosystems*, *7*, Q11007. https://doi.org/10.1029/2006GC001248

Montelli, R., Nolet, G., Masters, G., Dahlen, F. A., & Hung, S.-H. (2004). Global P and PP traveltime tomography: Rays versus waves. *Geophysical Journal International*, *158*(2), 637–654. https://doi.org/10.1111/j.1365-246X.2004.02346.x

Mooney, W. D., Artemieva, I., Detweiler, S. T., Billen, M., & Leveque, J.-J. (2003). Supplementing ground truth data with shear wave velocity, seismic attenuation, and thermal structure of the continental lithosphere. Proceedings of the 25th Seismic Research Review - Nuclear Explosion Monitoring: Building the knowledge base, 83–97

Moucha, R., & Forte, A. M. (2011). Changes in African topography driven by mantle convection. *Nature Geoscience*, *4*, 707–712. https://doi.org/10.1038/NGEO1235

Mulibo, G. D., & Nyblade, A. A. (2013a). The P and S wave velocity structure of the mantle beneath eastern Africa and the African superplume anomaly. *Geochemistry, Geophysics, Geosystems*, *14*, 2696–2715. https://doi.org/10.1002/ggge.20150

Mulibo, G. D., & Nyblade, A. A. (2013b). Mantle transition zone thinning beneath eastern Africa: Evidence for a whole-mantle superplume structure. *Geophysical Research Letters*, *40*, 3562–3566. https://doi.org/10.1002/grl.50694

Müller, R. D., Sdrolias, M., Gaina, C., Steinberger, B., & Heine, C. (2008). Long-term sea-level fluctuations driven by ocean basin dynamics. *Science*, *319*(5868), 1357–1362. https://doi.org/10.1126/science.1151540

National Observatory of Athens, Institute of Geodynamics, Athens (1997). National observatory of Athens seismic network, international federation of digital seismograph networks, Other/Seismic Network. https://doi.org/10.7914/SN/HL

Nita, B., Maurya, S., & Montagner, J.-P. (2016). Anisotropic tomography of the European lithospheric structure from surface wave studies. *Geochemistry, Geophysics, Geosystems*, *17*, 2015–2033. https://doi.org/10.1002/2015GC006243

Njome, M. S., & de Wit, M. J. (2014). The Cameroon Line: Analysis of an intraplate magmatic province transecting both oceanic and continental lithospheres: Constraints controversies and models. *Earth-Science Reviews*, *139*, 168–194. https://doi.org/10.1016/j.earscirev.2014.09.003

Nolet, G., & Mueller, S. (1982). A model for the deep structure of the East African Rift System from simultaneous inversion of teleseismic data. *Tectonophysics*, *84*(2-4), 151–178. https://doi.org/10.1016/0040-1951(82)90158-5

Nyblade, A. (2007). AfricaArray, international federation of digital seismograph networks, Other/Seismic Network. https://doi.org/10.7914/SN/ZP_2007

Nyblade, A. A. (2011). The upper-mantle low-velocity anomaly beneath Ethiopia, Kenya, and Tanzania: Constraints on the origin of the African superswell in eastern Africa and plate versus plume models of mantle dynamics. In L. Beccaluva, G. Bianchini, & M. Wilson (Eds.), *Volcanism and evolution of the African lithosphere*, *Geological Society of America Special Paper* (Vol. 478, pp. 1–14). https://doi.org/10.1130/2011.2478(03)

Nyblade, A. A., & Brazier, R. A. (2002). Precambrian lithospheric controls on the development of the East African rift system. *Geology*, *30*(8), 755–758. https://doi.org/10.1130/0091-7613(2002)030<0755:PLCOTD>2.0.CO;2

Nyblade, A. A., Owens, T. J., Gurrola, H., Ritsema, J., & Langston, C. A. (2000). Seismic evidence for a deep upper mantle thermal anomaly beneath east Africa. *Geology*, *28*(7), 599–602. https://doi.org/10.1130/0091-7613(2000)28<599:SEFADU>2.0.CO;2

Nyblade, A. A., & Robinson, S. W. (1994). The African superswell. *Geophysical Research Letters*, *21*(9), 765–768. https://doi.org/10.1029/94GL00631

O'Donnell, J. P., Adams, A., Nyblade, A. A., Mulibo, G. D., & Tugume, F. (2013). The uppermost mantle shear wave velocity structure of eastern Africa from Rayleigh wave tomography: Constraints on rift evolution. *Geophysical Journal International*, *194*(2), 961–978. https://doi.org/10.1093/gji/ggt135

O'Donnell, J. P., Selway, K., Nyblade, A. A., Brazier, R. A., El Tahir, N., & Durrheim, R. J. (2016). Thick lithosphere, deep crustal earthquakes and no melt: A triple challenge to understanding extension in the western branch of the East African Rift. *Geophysical Journal International*, *204*(2), 985–998. https://doi.org/10.1093/gji/ggv492

Ojo, A. O., Ni, S., Chen, H., & Xie, J. (2018). Crust-mantle coupling mechanism in Cameroon, West Africa, revealed by 3D S-wave velocity and azimuthal anisotropy. *Physics of the Earth and Planetary Interiors*, *274*, 195–213. https://doi.org/10.1016/j.pepi.2017.12.006

Paige, C. C., & Saunders, M. A. (1982). LSQR: An algorithm for sparse linear equations and sparse least squares. *ACM Transactions on Mathematical Software*, *8*(1), 43–71. https://doi.org/10.1145/355984.355989

Pasyanos, M. E., & Nyblade, A. A. (2007). A top to bottom lithospheric study of Africa and Arabia. *Tectonophysics*, *444*(1-4), 27–44. https://doi.org/10.1016/j.tecto.2007.07.008

Pasyanos, M. E., & Walter, W. R. (2002). Crust and upper-mantle structure of North Africa, Europe and the Middle East from inversion of surface waves. *Geophysical Journal International*, *149*(2), 463–481. https://doi.org/10.1046/j.1365-246X.2002.01663.x

Penn State University (2004). AfricaArray, international federation of digital seismograph networks, Other/Seismic Network. https://doi.org/10.7914/SN/AF

Porada, H. (1989). Pan-African rifting and orogenesis in southern to equatorial Africa, and eastern Brazil. *Precambrian Research*, *44*(2), 103–136. https://doi.org/10.1016/0301-9268(89)90078-8

Pratt, M. J., Wysession, M. E., Aleqabi, G., Wiens, D. A., Nyblade, A. A., Shore, P., Rambolamanana, G., et al. (2017). Shear velocity structure of the crust and upper mantle of Madagascar derived from surface wave tomography. *Earth and Planetary Science Letters*, *458*, 405–417. https://doi.org/10.1016/j.epsl.2016.10.041

Priestley, K., & McKenzie, D. (2006). The thermal structure of the lithosphere from shear wave velocities. *Earth and Planetary Science Letters*, *244*(1-2), 285–301. https://doi.org/10.1016/j.epsl.2006.01.008

Priestley, K., McKenzie, D., Debayle, E., & Pilidou, S. (2008). The African upper mantle and its relationship to tectonics and surface geology. *Geophysical Journal International*, *175*(3), 1108–1126. https://doi.org/10.1111/j.1365-246X.2008.03951.x

Rader, E., Emry, E., Schmerr, N., Frost, D., Cheng, C., Menard, J., Yu, C.-Q., et al. (2015). Characterization and petrological constraints of the midlithospheric discontinuity. *Geochemistry, Geophysics, Geosystems*, *16*, 3484–3504. https://doi.org/10.1002/2015GC005943

Raveloson, A., Nyblade, A., Fishwick, S., Mangongola, A., & Master, S. (2015). The upper mantle seismic velocity structure of south-central Africa and seismic architecture of Precambrian lithosphere beneath the Congo Basin. In M. J. de Wit, F. Guillocheau, & M. C. J. de Wit (Eds.), *Geology and Resource Potential of the Congo Basin, Regional Geology Reviews*, (pp. 3–18). Berlin, Heidelberg: Springer. https://doi.org/10.1007/978-3-642-29482-2_1

Rawlinson, N., Fichtner, A., Sambridge, M., & Young, M. K. (2014). Seismic tomography and the assessment of uncertainty. *Advances in Geophysics*, *55*, 1–76. https://doi.org/10.1016/bs.agph.2014.08.001

Reed, C. A., Gao, S. S., Liu, K. H., & Yu, Y. (2016). The mantle transition zone beneath the Afar depression and adjacent regions: Implications for mantle plumes and hydration. *Geophysical Journal International*, *205*(3), 1756–1766. https://doi.org/10.1093/gji/ggw116

Reed, C. A., Liu, K. H., Chindandali, P. R. N., Massingue, B., Mdala, H., Mutamina, D., Yu, Y., et al. (2016). Passive rifting of thick lithosphere in the southern East African Rift: Evidence from mantle transition zone discontinuity topography. *Journal of Geophysical Research: Solid Earth*, *121*, 8068–8079. https://doi.org/10.1002/2016JB013131

Reusch, A. M., Nyblade, A. A., Wiens, D. A., Shore, P. J., Ateba, B., Tabod, C. T., & Nnange, J. M. (2010). Upper mantle structure beneath Cameroon from body wave tomography and the origin of the Cameroon Volcanic Line. *Geochemistry, Geophysics, Geosystems*, *11*, Q10W07. https://doi.org/10.1029/2010GC003200

Rhie, J., & Romanowicz, B. (2004). Excitation of Earth's continuous free oscillations by atmosphere-ocean-seafloor coupling. *Nature*, *431*, 552–556. https://doi.org/10.1038/nature02942

Rino, S., Kon, Y., Sato, W., Maruyama, S., Santosh, M., & Zhao, D. (2008). The Grenvillian and Pan-African orogens: World's largest orogenies through geologic time, and their implications on the origin of superplume. *Gondwana Research*, *14*(1-2), 51–72. https://doi.org/10.1016/j.gr.2008.01.001

Ritsema, J., Deuss, A., van Heijst, H. J., & Woodhouse, J. H. (2011). S40RTS: A degree-40 shear-velocity model for the mantle from new Rayleigh wave dispersion, teleseismic traveltime and normal-mode splitting function measurements. *Geophysical Journal International*, *184*(3), 1223–1236. https://doi.org/10.1111/j.1365-246X.2010.04884.x

Ritsema, J., Nyblade, A. A., Owens, T. J., Langston, C. A., & VanDecar, J. C. (1998). Upper mantle seismic velocity structure beneath Tanzania, east Africa: Implications for the stability of cratonic lithosphere. *Journal of Geophysical Research*, *103*(B9), 21,201–21,213. https://doi.org/10.1029/98JB01274

Ritsema, J., & van Heijst, H. (2000). New seismic model of the upper mantle beneath Africa. *Geology*, *28*(1), 63–66. https://doi.org/10.1130/0091-7613(2000)28<63:NSMOTU>2.0.CO;2

Ritsema, J., van Heijst, H. J., & Woodhouse, J. H. (1999). Complex shear wave velocity structure imaged beneath Africa and Iceland. *Science*, *286*(5446), 1925–1928. https://doi.org/10.1126/science.286.5446.1925

Roberts, G. G., & White, N. (2010). Estimating uplift rate histories from river profiles using African examples. *Journal of Geophysical Research*, *115*, B02406. https://doi.org/10.1029/2009JB006692

Rondenay, S. (2006). Multi-disciplinary Experiments for Dynamic Understanding of Subduction under the Aegean Sea, International Federation of Digital Seismograph Networks, Other/Seismic Network. https://doi.org/10.7914/SN/XS_2006
Rooney, T. O., Herzberg, C., & Bastow, I. D. (2012). Elevated mantle temperature beneath East Africa. *Geology*, *40*(1), 27–30. https://doi.org/10.1130/G32382.1
Rychert, C. A., Hammond, J. O. S., Harmon, N., Kendall, J. M., Keir, D., Ebinger, C., Bastow, I. D., et al. (2012). Volcanism in the Afar Rift sustained by decompression melting with minimal plume influence. *Nature Geoscience*, *5*, 406–409. https://doi.org/10.1038/NGEO1455
Saalmann, K., Mänttäri, I., Nyakecho, C., & Isabirye, E. (2016). Age, tectonic evolution and origin of the Aswa Shear Zone in Uganda: Activation of an oblique ramp during convergence in the East African Orogen. *Journal of African Earth Sciences*, *117*, 303–330. https://doi.org/10.1016/j.jafrearsci.2016.02.002
Saki, M., Thomas, C., Nippress, S. E. J., & Lessing, S. (2015). Topography of upper mantle seismic discontinuities beneath the North Atlantic: The Azores, Canary and Cape Verde plumes. *Earth and Planetary Science Letters*, *409*, 193–202. https://doi.org/10.1016/j.epsl.2014.10.052
Sarafian, E., Evans, R. L., Abdelsalam, M. G., Atekwana, E., Elsenbeck, J., Jones, A. G., & Chikambwe, E. (2018). Imaging Precambrian lithospheric structure in Zambia using electromagnetic methods. *Gondwana Research*, *54*, 38–49. https://doi.org/10.1016/j.gr.2017.09.007
Savage, B., Covellone, B. M., & Shen, Y. (2017). Wave speed structure of the eastern North American margin. *Earth and Planetary Science Letters*, *459*, 394–405. https://doi.org/10.1016/j.epsl.2016.11.028
Schaeffer, A. J., & Lebedev, S. (2013). Global shear speed structure of the upper mantle and transition zone. *Geophysical Journal International*, *194*, 417–449. https://doi.org/10.1093/gji/ggt095
Scripps Institution of Oceanography (1986). IRIS/IDA seismic network, international federation of digital seismograph networks, Other/Seismic Network. https://doi.org/10.7914/SN/II
Sebai, A., Stutzmann, E., Montagner, J.-P., Sicilia, D., & Beucler, E. (2006). Anisotropic structure of the African upper mantle from Rayleigh and Love wave tomography. *Physics of the Earth and Planetary Interiors*, *155*(1-2), 48–62. https://doi.org/10.1016/j.pepi.2005.09.009
Selway, K., Ford, H., & Kelemen, P. (2015). The seismic mid-lithospheric discontinuity. *Earth and Planetary Science Letters*, *414*, 45–57. https://doi.org/10.1016/j.epsl.2014.12.029
Shapiro, N. M., Campillo, M., Stehly, L., & Ritzwoller, M. H. (2005). High-resolution surface-wave tomography from ambient seismic noise. *Science*, *307*(5715), 1615–1618. https://doi.org/10.1126/science.1108339
Shapiro, S. S., Hager, B. H., & Jordan, T. H. (1999). Stability and dynamics of the continental tectosphere. *Lithos*, *48*, 115–133. https://doi.org/10.1016/S0419-0254(99)80008-1
Shellnutt, J. G., Lee, T.-Y., Torng, P.-K., Yang, C.-C., & Lee, Y.-H. (2016). Later Cretaceous intraplate silicic volcanic rocks from the Lake Chad region: An extension of the Cameroon volcanic line? *Geochemistry, Geophysics, Geosystems*, *17*, 2803–2824. https://doi.org/10.1002/2016GC006298
Shen, W., Wiens, D. A., Stern, T., Anandakrishnan, S., Aster, R. C., Dalziel, I., Hansen, S., et al. (2018). Seismic evidence for lithospheric foundering beneath the southern Transantarctic Mountains, Antarctica. *Geology*, *46*(1), 71–74. https://doi.org/10.1130/G39555.1
Shen, Y., Ren, Y., Gao, H., & Savage, B. (2012). An improved method to extract very-broadband empirical green's functions from ambient seismic noise. *Bulletin of the Seismological Society of America*, *102*(4), 1872–1877. https://doi.org/10.1785/0120120023
Shen, Y. & Zhang, W. (2012). Full-wave tomography of the eastern hemisphere, Proceedings of the 2012 Monitoring Research Review: Ground-based Nuclear Explosion Monitoring Technologies, 121-129.
Sicilia, D., Montagner, J.-P., Cara, M., Stutzmann, E., Debayle, E., Lépine, J.-C., Lévêque, J.-J., et al. (2008). Upper mantle structure of shear-waves velocities and stratification of anisotropy in the Afar Hotspot region. *Tectonophysics*, *462*(1-4), 164–177. https://doi.org/10.1016/j.tecto.2008.02.016
Silver, P. (1997). A multidisciplinary experiment across the Kaapvaal Craton, International Federation of Digital Seismograph Networks, Other/Seismic Network. doi:https://doi.org/10.7914/SN/XA_1997
Simmons, N. A., Forte, A. M., Boschi, L., & Grand, S. P. (2010). GyPSuM: A joint tomographic model of mantle density and seismic wave speeds. *Journal of Geophysical Research*, *115*, B12310. https://doi.org/10.1029/2010JB007631
Simmons, N. A., Myers, S. C., Johannesson, G., & Matzel, E. (2012). LLNL-G3Dv3: Global P wave tomography model for improved regional and teleseismic travel time prediction. *Journal of Geophysical Research*, *117*, B10302. https://doi.org/10.1029/2012JB009525
Slack, P. D., Davis, P. M., Dahlheim, H. A., Glahn, A., Ritter, J. R. R., Green, W. V., Maguire, P. K. H., et al. (1994). Attenuation and velocity of P-waves in the mantle beneath the East African Rift, Kenya. *Tectonophysics*, *236*(1-4), 331–358. https://doi.org/10.1016/0040-1951(94)90183-X
Snyder, D. B., Humphreys, E., & Pearson, D. G. (2017). Construction and destruction of some North American cratons. *Tectonophysics*, *694*, 464–485. https://doi.org/10.1016/j.tecto.2016.11.032
Sodoudi, F., Yuan, X., Kind, R., Lebedev, S., Adam, J. M.-C., Kästle, E., & Tilmann, F. (2013). Seismic evidence for stratification in composition and anisotropic fabric within the thick lithosphere of Kalahari Craton. *Geochemistry, Geophysics, Geosystems*, *14*, 5393–5412. https://doi.org/10.1002/2013GC004955
Stehly, L., Campillo, M., & Shapiro, N. M. (2006). A study of the seismic noise from its long-range correlation properties. *Journal of Geophysical Research*, *111*, B10306. https://doi.org/10.1029/2005JB004237
Sun, M., Liu, K. H., Fu, X., & Gao, S. S. (2017). Receiver function imaging of mantle transition zone discontinuities beneath the Tanzania Craton and adjacent segments of the East African Rift System. *Geophysical Research Letters*, *44*, 12,116–12,124. https://doi.org/10.1002/2017GL075485
Tang, Y.-J., Zhang, H.-F., Ying, J.-F., & Su, B.-X. (2013). Widespread refertilization of cratonic and circum-cratonic lithospheric mantle. *Earth-Science Reviews*, *118*, 45–68. https://doi.org/10.1016/j.earscirev.2013.01.004
Tape, C., Liu, Q., Maggi, A., & Tromp, J. (2010). Seismic tomography of the southern California crust based on spectral-element and adjoint methods. *Geophysical Journal International*, *180*(1), 433–462. https://doi.org/10.1111/j.1365-246X.2009.04429.x
Tape, C., Liu, Q., & Tromp, J. (2007). Finite-frequency tomography using adjoint methods—Methodology and examples using membrane surface waves. *Geophysical Journal International*, *168*(3), 1105–1129. https://doi.org/10.1111/j.1365-246X.2006.03191.x
Thompson, D. A., Hammond, J. O. S., Kendall, J.-M., Stuart, G. W., Hellfrich, G. R., Keir, D., Ayele, A., et al. (2015). Hydrous upwelling across the mantle transition zone beneath the Afar Triple Junction. *Geochemistry, Geophysics, Geosystems*, *16*, 834–846. https://doi.org/10.1002/2014GC005648
Tokam, A.-P. K., Tabod, C. T., Nyblade, A. A., Julià, J., Wiens, D. A., & Pasyanos, M. E. (2010). Structure of the crust beneath Cameroon, West Africa, from the joint inversion of Rayleigh wave group velocities and receiver functions. *Geophysical Journal International*, *183*(2), 1061–1076. https://doi.org/10.1111/j.1365-246X.2010.04776.x
Tosi, N., & Yuen, D. A. (2011). Bent-shaped plumes and horizontal channel flow beneath the 660 km discontinuity. *Earth and Planetary Science Letters*, *312*, 348–359. https://doi.org/10.1016/j.epsl.2011.10.015

van Wijk, J. W., Baldridge, W. S., van Hunen, J., Goes, S., Aster, R., Coblentz, D. D., Grand, S. P., et al. (2010). Small-scale convection at the edge of the Colorado Plateau: Implications for topography, magmatism, and evolution of the Proterozoic lithosphere. *Geology*, *38*(7), 611–614. https://doi.org/10.1130/G31031.1

Venkataraman, A., Nyblade, A. A., & Ritsema, J. (2004). Upper mantle Q and thermal structure beneath Tanzania, East Africa from teleseismic P wave spectra. *Geophysical Research Letters*, *31*, L15611. https://doi.org/10.1029/2004GL020351

Vinnik, L., Chevrot, S., & Montagner, J.-P. (1997). Evidence for a stagnant plume in the transition zone? *Geophysical Research Letters*, *24*(9), 1007–1010. https://doi.org/10.1029/97GL00786

Walford, H. L., & White, N. J. (2005). Constraining uplift and denudation of West African continental margin by inversion of stacking velocity data. *Journal of Geophysical Research*, *110*, B04403. https://doi.org/10.1029/2003JB002893

Walker, R. T., Telfer, M., Kahle, R. L., Dee, M. W., Kahle, B., Schwenninger, J.-L., Sloan, R. A., et al. (2016). Rapid mantle-driven uplift along the Angolan margin in the late Quaternary. *Nature Geoscience*, *9*, 909–914. https://doi.org/10.1038/NGEO2835

Wang, H., van Hunen, J., & Pearson, D. G. (2015). The thinning of subcontinental lithosphere: The roles of plume impact and metasomatic weakening. *Geochemistry, Geophysics, Geosystems*, *16*, 1156–1171. https://doi.org/10.1002/2015GC005784

Weeraratne, D. S., Forsyth, D. W., Fischer, K. M., & Nyblade, A. A. (2003). Evidence for an upper mantle plume beneath the Tanzanian craton from Rayleigh wave tomography. *Journal of Geophysical Research*, *108*(B9), 2427. https://doi.org/10.1029/2002JB002273

West, J. D., Fouch, M. J., Roth, J. B., & Elkins-Tanton, L. T. (2009). Vertical mantle flow associated with a lithospheric drip beneath the Great Basin. *Nature Geoscience*, *2*, 439–444. https://doi.org/10.1038/NGEO526

Wiens, D. & Nyblade, A. (2005). Broadband seismic investigation of the Cameroon Volcanic Line, international federation of digital seismograph networks, other/seismic network. https://doi.org/10.7914/SN/XB_2005

Wirth, E. A., & Long, M. D. (2014). A contrast in anisotropy across the mid-lithospheric discontinuities beneath the central United States—A relic of craton formation. *Geology*, *42*(10), 851–854. https://doi.org/10.1130/G35804.1

Wysession, M., Wiens, D. & Nyblade, A. (2011). Investigation of sources of intraplate volcanism using PASSCAL broadband instruments in Madagascar, the Comores, and Mozambique, International Federation of Digital Seismograph Networks, Other/Seismic Network. https://doi.org/10.7914/SN/XV_2011

Wysession, M.E., Pratt, M.J., Tsiriandrimanana, R., Andriampenomanana Ny Ony, F.S.T., Nyblade, A., Durrheim, R.J., Tilmann, F.J., et al. (2017). Normal-faulting in Madagascar: Another round of continental rifting?. American Geophysical Union, Fall Meeting 2017, abstract #T41E-03, 2017AGUFM.T41E..03W.

Xu, Y.-G. (2001). Thermo-tectonic destruction of the Archaean lithospheric keel beneath the Sino-Korean Craton in China: Evidence, timing, and mechanism. *Physics and Chemistry of the Earth, Part A: Solid Earth and Geodesy*, *26*(9-10), 747–757. https://doi.org/10.1016/S1464-1895(01)00124-7

Yao, Z., Mooney, W. D., Zahran, H. M., & El-Hadidy Youssef, S. (2017). Upper mantle velocity structure beneath the Arabian shield from Rayleigh surface wave tomography and its implications. *Journal of Geophysical Research: Solid Earth*, *122*, 6552–6568. https://doi.org/10.1002/2016JB013805

Yu, Y., Liu, K. H., Moidaki, M., Reed, C. A., & Gao, S. S. (2015). No thermal anomalies in the mantle transition zone beneath an incipient continental rift: Evidence from the first receiver function study across the Okavango Rift Zone, Botswana. *Geophysical Journal International*, *202*(2), 1407–1418. https://doi.org/10.1093/gji/ggv229

Yuan, H., & Romanowicz, B. (2010). Lithospheric layering in the North American craton. *Nature*, *466*, 1063–1068. https://doi.org/10.1038/nature09332

Zhang, S.-H., Zhao, Y., Davis, G. A., Ye, H., & Wu, F. (2014). Temporal and spatial variations of Mesozoic magmatism and deformation in the North China Craton: Implications for lithospheric thinning and decratonization. *Earth-Science Reviews*, *131*, 49–87. https://doi.org/10.1016/j.earscirev.2013.12.004

Zhang, W., & Shen, Y. (2010). Unsplit complex frequency-shifted PML implementation using auxiliary differential equations for seismic wave modeling. *Geophysics*, *75*(4), T141–T154. https://doi.org/10.1190/1.3463431

Zhang, W., Shen, Y., & Zhao, L. (2012). Three-dimensional anisotropic seismic wave modelling in spherical coordinates by a collocated-grid finite-difference method. *Geophysical Journal International*, *188*(3), 1359–1381. https://doi.org/10.1111/j.1365-246X.2011.05331.x

Zhao, L., Jordan, T. H., Olsen, K. B., & Chen, P. (2005). Fréchet kernels for imaging regional Earth structure based on three-dimensional reference models. *Bulletin of the Seismological Society of America*, *95*(6), 2066–2080. https://doi.org/10.1785/0120050081

Zhou, Y., Liu, Q., & Tromp, J. (2011). Surface wave sensitivity: Mode summation versus adjoint SEM. *Geophysical Journal International*, *187*(3), 1560–1576. https://doi.org/10.1111/j.1365-246X.2011.05212.x